

Spontaneous Emission of Internal Waves by a Radiative Instability[©]

SUBHAJIT KAR,^a ROY BARKAN,^{a,b} JAMES C. MCWILLIAMS,^b AND M. JEROEN MOLEMAKER^b

^a Porter School of the Environment and Earth Sciences, Tel Aviv University, Ramat Aviv, Israel

^b Department of Atmospheric and Oceanic Sciences, University of California, Los Angeles, Los Angeles, California

(Manuscript received 16 September 2024, in final form 17 January 2025, accepted 3 February 2025)

ABSTRACT: The spontaneous emission of internal waves (IWs) from balanced mesoscale eddies has been previously proposed to provide a source of oceanic IW kinetic energy (KE). This study examines the mechanisms leading to the spontaneous emission of the spiral-shaped IWs from an anticyclonic eddy with an order-one Rossby number, using a high-resolution numerical simulation of a flat-bottomed, wind-forced, reentrant channel flow configured to resemble the Antarctic Circumpolar Current. It is demonstrated that the IWs are spontaneously generated as a result of a loss of balance process that is concentrated at the eddy edge and then radiates radially outward. A 2D linear stability analysis of the eddy shows that the spontaneous emission arises from a radiative instability which involves an interaction between a vortex Rossby wave supported by the radial gradient of potential vorticity and an outgoing IW. This particular instability occurs when the perturbation frequency is superinertial. This finding is supported by a KE analysis of the unstable modes and the numerical solution, where it is shown that the horizontal shear production provides the source of the perturbation KE. Furthermore, the horizontal length scale and frequency of the most unstable mode from the stability analysis agree well with those of the spontaneously emitted IWs in the numerical solution.

SIGNIFICANCE STATEMENT: Spontaneous emission of internal waves (IWs) describes a process by which large-scale, slow oceanic currents can spontaneously emit IWs. Recent observations and numerical studies suggest that spontaneous IW emission can provide an important IW energy source. Identifying the mechanisms responsible for spontaneous IW emission is therefore of utmost importance because IW breaking has crucial effects on the oceanic large-scale circulation. This study examines the spontaneous emission of IWs from a numerically simulated anticyclonic eddy. We show that the emission process results from radiative instability when the perturbation frequency is larger than the Coriolis frequency. This instability mechanism can be significant across the oceans for flow structures with order-one Rossby numbers (a measure of flow nonlinearity).

KEYWORDS: Eddies; Instability; Internal waves

1. Introduction

Internal waves (IWs) are ubiquitous in the ocean, and their breaking drives turbulent mixing that shapes large-scale circulation patterns and the distribution of heat and carbon in the climate system (Munk and Wunsch 1998; Whalen et al. 2020). They represent a large energy reservoir, with about 1 terawatt (TW) converted from barotropic tides (Egbert and Ray 2000; Nycander 2005), and another 0.3–1.4 TW converted into near-inertial IWs, mainly from high-frequency wind forcing (Alford 2003; Rimac et al. 2013).

Another possible mechanism for IW generation that has been proposed is termed spontaneous emission—a process that describes the spontaneous generation of IWs from so-called balanced motions (see Vanneste 2013 and references therein). These balanced motions satisfy the *invertibility principle of potential vorticity* (PV)—at a given instant, all dynamical fields (e.g., velocity, density) can be deduced by inverting

the PV without the need to time evolve each of the fields separately (Hoskins et al. 1985). A classic example is the quasigeostrophic (QG) model (Pedlosky 2013), which is quite successful in describing the dynamics of oceanic mesoscale eddies, typically characterized by small Rossby numbers ($\text{Ro} \ll 1$) and large Richardson numbers ($\text{Ri} \gg 1$).

Ford (1994a) and Ford et al. (2000) demonstrated the analogy between spontaneous emission of IWs from a balanced flow and Lighthill radiation of acoustic waves from a turbulent flow (Lighthill 1954). Vanneste and Yavneh (2004) and Vanneste (2008) showed that in the low-Ro regime, spontaneous emission is expected to be exponentially small. Conversely, Williams et al. (2008) found in laboratory experiments that the amplitude of the spontaneously emitted IWs depends linearly on Ro. In both paradigms, these previous findings suggest that spontaneous emission could be significant in high-Ro flows.

Indeed, Shakespeare and Taylor (2014) showed analytically that the spontaneous emission from strained fronts could be significant for large strain values, representing an $O(1)$ Rossby number regime. Later, Nagai et al. (2015) performed an idealized simulation of a Kuroshio Front and demonstrated significant spontaneous emission of IW energy from the front. The emitted IWs were eventually reabsorbed into the mean flow at depth, thereby redistributing the balanced flow energy rather than providing a significant sink. Using high-resolution numerical

[©] Supplemental information related to this paper is available at the Journals Online website: <https://doi.org/10.1175/JPO-D-24-0185.s1>.

Corresponding author: Subhajit Kar, subhajitkar@mail.tau.ac.il

simulations of an idealized channel flow, [Shakespeare and Hogg \(2017\)](#) also reported spontaneous emission of IWs from surface fronts, which were further amplified at depth through energy exchanges with the mean flow.

Direct observational evidence of spontaneous emission in the ocean is scarce, likely due to the difficulty in eliminating other IW generation mechanisms using sparse measurements. [Alford et al. \(2013\)](#) measured the rate of generation of IWs from a subtropical frontal jet in the northern Pacific Ocean to be $0.6\text{--}2.4 \text{ mW m}^{-2}$, which leads to a source of about $0.2\text{--}0.9\text{-TW}$ IW energy, when extrapolated to the global ocean. This rough evaluation is comparable to the estimate of wind-forced near-inertial IWs, thereby suggesting that spontaneous emission could be significant to the ocean's kinetic energy (KE) budget. Using synthetic aperture radar and in situ measurements, [Johannessen et al. \(2019\)](#) showed evidence of spontaneous emission of IWs from a mesoscale, baroclinic anticyclonic eddy in the Greenland Sea (at the latitude of $\sim 78^\circ\text{N}$) with a horizontal scale of 1 km. Furthermore, [Chunchuzov et al. \(2021\)](#) used high-resolution infrared imaging to observe the emission of spiral-shaped IWs, with a horizontal scale of $0.4\text{--}1 \text{ km}$, originating from the edge of a high Rossby number submesoscale cyclonic eddy near Catalina Island.

In this article, we investigate the spontaneous emission of spiral-shaped IWs from an anticyclonic eddy of $O(1)$ Rossby number, using a high-resolution numerical simulation of a statistically equilibrated channel flow. We show that the spontaneous emission is directly linked to a loss of balance (LOB) process that results from a radiative instability of the eddy. This radiative instability mechanism closely follows the one described in [Schechter and Montgomery \(2004\)](#), hereinafter **SM04**, in the context of atmospheric cyclones. **SM04** demonstrated that an idealized barotropic Rankine vortex can become unstable and emit IWs due to the interaction between a vortex Rossby wave, which is supported by the radial gradient of the mean flow PV, and an outward-propagating IW. In this article, we present the first demonstration of this instability mechanism in a forced dissipative numerical solution.

The article is organized as follows. In [section 2](#), we describe the numerical setup used to study the spontaneous emission of IWs from the eddy. The quantification of LOB of the mean flow and the generation and propagation of the radiated IWs are discussed in [section 3](#). In [section 4](#), we examine possible mechanisms leading to LOB and spontaneous emission. The setup and methodology used to carry out a 2D linear stability analysis of the eddy circulation are described in [section 5](#). In [section 6](#), we present the results of the stability analysis and compare them with the numerical solution. The instability mechanism is discussed in [section 7](#), and in [section 8](#), we summarize our findings and their implications for realistic ocean scenarios.

2. Numerical setup

The numerical simulations are performed using `flow_solve` ([Winters and de la Fuente 2012](#)), a pseudospectral, nonhydrostatic, Boussinesq solver. The setup consists of a reentrant channel flow on an f plane over which wind blows to mimic an

idealized configuration of the Antarctic Circumpolar Current (ACC), with an initial stratification profile based on observations from the Southern Ocean ([Garabato et al. 2004](#)). Without loss of generality, the Coriolis frequency $f > 0$ and the value is fixed to $f = 1.2 \times 10^{-4} \text{ s}^{-1}$. The domain sizes in the zonal, meridional, and vertical ($\hat{x}, \hat{y}, \hat{z}$) are $L_x = 200 \text{ km}$, $L_y = 200 \text{ km}$, and $H = 2 \text{ km}$, respectively. The boundary conditions are periodic in the zonal direction, free-slip wall in the meridional direction, and free-slip rigid lid in the vertical direction.

The numerical analysis shown in this manuscript is based on one of the simulations previously discussed in [Barkan et al. \(2017\)](#). The simulation is forced by a steady wind stress τ_s of the form:

$$\tau_s(y) = \tau_0 \sin^2\left(\frac{\pi y}{L_y}\right)\hat{x}, \quad (1)$$

where $\rho_0 \tau_0 = 0.1 \text{ N m}^{-2}$ and the reference density $\rho_0 = 10^3 \text{ kg m}^{-3}$. The wind stress is applied as a body force confined to the upper $\sim 80 \text{ m}$, representing an effective mixed layer depth. This wind forcing drives a zonal jet (i.e., an idealized “ACC”) and induces Ekman upwelling and downwelling that tilt the initially flat isopycnals, leading to baroclinic instability and the subsequent formation of mesoscale baroclinic eddies.

This system initially spins up in a coarser resolution simulation until a statistical steady state is reached. Following this, a higher-resolution simulation is initiated and run for 4 months [for further detail, the reader is referred to [Barkan et al. \(2017\)](#)]. The hourly output of the last month is used for the analysis in this study. A representative snapshot of the vertical component of vorticity at the surface shows a large anticyclonic eddy, two cyclonic eddies, and smaller-scale fronts and filaments with $O(1)$ Rossby numbers ([Fig. 1a](#)). The signature of IWs can be easily visualized in the vertical velocity field, which is typically much larger than that associated with the eddy circulations. The corresponding vertical velocity in the vicinity of the anticyclonic eddy at 500-m depth shows spiral-shaped structures that originate near the edge of the eddy ([Fig. 1c](#)). The associated power spectral density of the vertical velocity suggests that the spiraling structures may be the signature of spontaneously emitted IWs with an $\approx 1.3f$ frequency ([Fig. 1b](#)). In what follows, we investigate the mechanisms leading to the spontaneous IW emission from this anticyclonic eddy.

Because the anticyclonic eddy is being translated by the idealized ACC in the x direction with a nearly constant speed of $U_{\text{ref}} = 0.26 \text{ m s}^{-1}$, we carry out the analysis that follows in the ACC reference frame:

$$X = x - U_{\text{ref}}t, Y = y, Z = z, \quad (2)$$

where (x, y, z) are the Cartesian coordinates of the numerical simulation.

Furthermore, to separate the spontaneously emitted IWs from the slowly evolving mean flow, we decompose any field ϕ , namely,

$$\phi = \bar{\phi} + \phi', \quad (3)$$

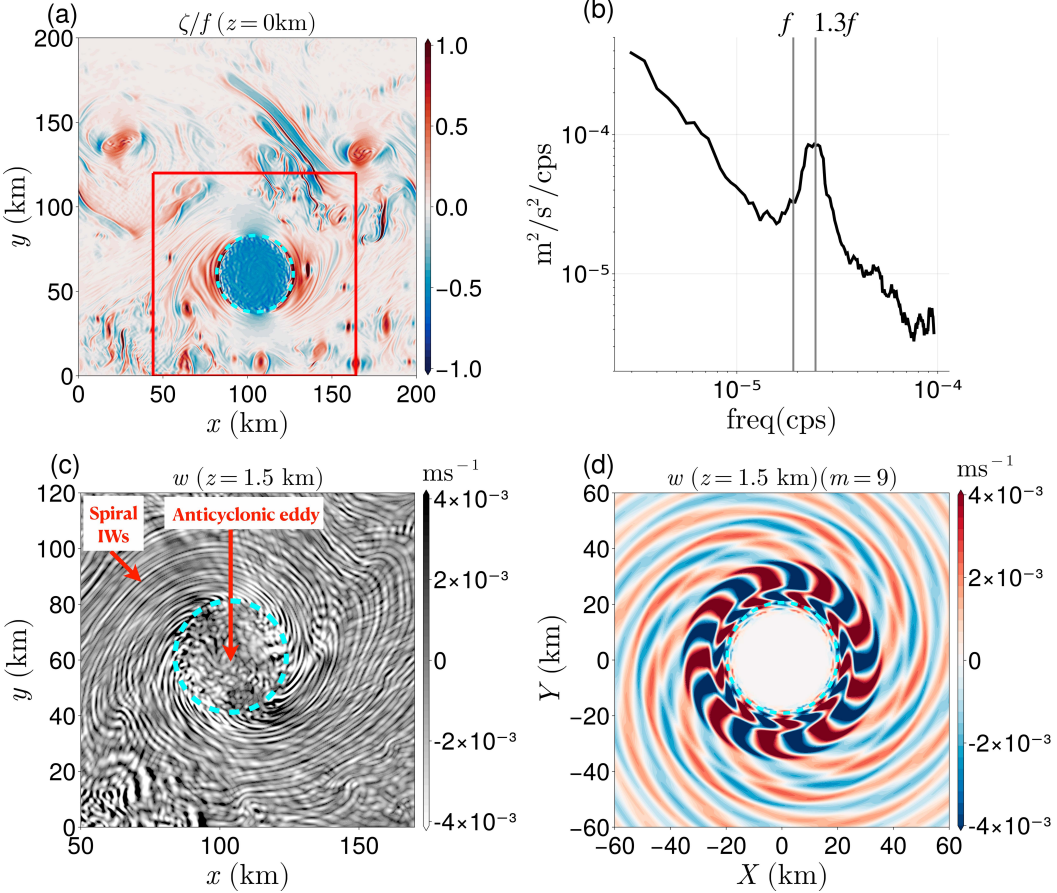


FIG. 1. (a) A representative surface snapshot of the vertical component of vorticity ζ (normalized by f). The red box region of size $(120 \text{ km} \times 120 \text{ km})$ is used to analyze IW generation and propagation from the anticyclonic eddy. (b) Vertical velocity w frequency spectra in a frame moving with the ACC [Eq. (2)]. The spectrum is computed in the red box region shown in (a), excluding the anticyclonic eddy region. The spectrum peaks approximately at $1.3f$. (c) A representative snapshot of the vertical velocity w at $z = 1.5 \text{ km}$ at the same time instance of the (a). The spiral-shaped IWs radiated from the edge of the eddy are visible. Reflection of the radiated IWs from the free-slip wall at $y = 0 \text{ km}$ is also visible. The dashed cyan lines in (a), (c), and (d) mark the radius $R = 20 \text{ km}$ of the eddy. Typically, the horizontal length scale of the emitted IWs is $\sim 4 \text{ km}$. (d) Solution of vertical velocity w obtained from 2D linear stability analysis of the eddy for the case of azimuthal wavenumber $m = 9$ (see section 5 for more details).

where the overline denotes a low-pass sixth-order Butterworth temporal filter with a frequency cutoff of $0.8f$ and the prime denotes the remaining IW field. The filtering is applied in the moving reference frame (X, Y, Z) to reduce the Doppler shifting effects (e.g., Rama et al. 2022).

Throughout the article, we used the notation $\langle \cdot \rangle$ to represent an average quantity, and the subscript of the notation denotes the average along that direction unless otherwise stated, for example,

$$\langle \phi \rangle_z = \frac{1}{H} \int_0^H \phi dz, \quad (4)$$

which denotes the vertical average of ϕ .

3. Evidence of loss of balance and spontaneous emission

To determine whether the IW signatures shown in Fig. 1c are indeed associated with an LOB in the anticyclonic eddy,

we diagnose the departure from the gradient wind balance (McWilliams 1985):

$$-\nabla_h \cdot (\mathbf{u}_h \cdot \nabla_h \mathbf{u}_h) + f\zeta = \nabla_h^2 p, \quad (5)$$

where $\nabla_h = (\partial_X, \partial_Y)$ is the horizontal gradient operator, $\mathbf{u}_h = (u, v)$ is the horizontal velocity vector, and p is the pressure. The associated LOB measure for a given flow field (\mathbf{u}_h, p) can be defined (Capet et al. 2008) as follows:

$$\epsilon(\mathbf{u}_h, p) = \frac{|\nabla_h \cdot (\mathbf{u}_h \cdot \nabla_h \mathbf{u}_h) - f\zeta + \nabla_h^2 p|}{|\nabla_h \cdot (\mathbf{u}_h \cdot \nabla_h \mathbf{u}_h)| + f|\zeta| + |\nabla_h^2 p| + \mu}, \quad (6)$$

where the term $\mu = f\zeta_{\text{rms}} + (\nabla_h^2 p)_{\text{rms}}$ is added to the denominator of Eq. (6) to eliminate the possibility of identifying weak flow regions as significantly unbalanced. The value of ϵ varies from 0 to 1, with $\epsilon = 0$ ($\epsilon = 1$) denoting fully balanced

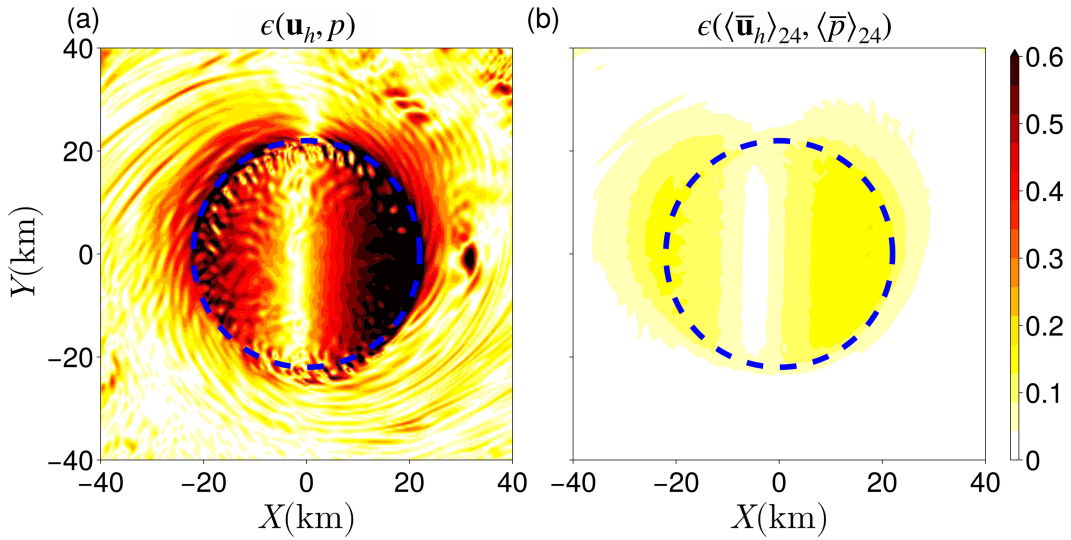


FIG. 2. (a) A representative surface snapshot of the LOB parameter ϵ [Eq. (6)], computed at the same time as is shown in Figs. 1a and 1b ϵ computed from the daily time average of the low-pass velocity and pressure field ($\langle \bar{u}_h \rangle_{24}, \langle \bar{p} \rangle_{24}$). The daily time average is used to smooth out any small-scale motions within the eddy that cannot be removed by the Eulerian temporal filter. The dashed blue line marks the edge of the anticyclonic eddy.

(unbalanced) motions. A representative snapshot of ϵ at the surface shows a significant imbalance around the edge of the anticyclonic eddy (Fig. 2a). Since the anticyclonic eddy is constantly being deformed by straining motions (note the cyclonic circulation pattern around its edge; Fig. 1a), it does not retain a perfectly circular shape, resulting in an asymmetric ϵ . More importantly, the motions leading to loss of balance are found to be quite rapid because the daily averaged low-pass velocity field is largely balanced (Fig. 2b). Hereinafter, we refer to this balanced flow as the *mean flow* or *basic state*. To denote it, we used the subscript “*m*,” which describes the daily average of the low-pass field.

To establish the connection between the rapid motions leading to LOB at the edge of the anticyclonic eddy and the spontaneous emission of IWs, we first compute the IW energy flux:

$$\mathbf{F} = \overline{\mathbf{u}' p'}, \quad (7)$$

where $\mathbf{u}' \equiv (u'_r, u'_\theta, w')$ and p' denote the IW velocity and pressure fields, respectively. These IW fluxes are computed in a cylindrical coordinate system (r, θ, z) centered around the anticyclonic eddy, with

$$r = \sqrt{X^2 + Y^2}, \quad \theta = \tan^{-1}(Y/r). \quad (8)$$

The temporal filter [Eq. (3)] is applied after removing the depth-averaged fields at each time instant.

The associated outward-propagating IW energy can be estimated using the azimuthally and vertically averaged radial energy flux, namely (Voelker et al. 2019),

$$\Phi_{IW}(r, t) = \frac{1}{H} \int_0^H \int_0^{2\pi} F_r r d\theta dz, \quad (9)$$

where $F_r = \overline{u'_r p'}$. Indeed, positive values of Φ_{IW} demonstrate that substantial IW energy radiates outward from the edge of the eddy (Fig. 3a), as is also visible in the depth-averaged energy flux vector (Fig. 3b). The sign change in Φ_{IW} , which occurs at the edge of the eddy, suggests that the spontaneously emitted IWs are generated near the edge of the eddy. Indeed, the azimuthal, vertical, and temporal average of the IW flux divergence,

$$\langle \nabla \cdot \mathbf{F} \rangle_{\theta, z, t} = \frac{1}{2\pi HT} \int_0^{2\pi} \int_0^H \int_0^T \frac{\partial}{\partial r} (r F_r) dt dz d\theta, \quad (10)$$

is small inside the eddy (the blue shaded region in Fig. 3c), peaks just outside it, and then decays to zero around $r = 30$ km. Further away from the eddy, the value of $\langle \nabla \cdot \mathbf{F} \rangle_{\theta, z, t}$ remains nearly zero, implying that $\partial/\partial r \langle r F_r \rangle_{\theta, z, t} \approx 0$. This suggests that the average radial energy flux $\langle F_r \rangle_{\theta, z, t}$ is proportional to r^{-1} , consistent with Fig. 3d.

4. Spontaneous emission mechanisms

Next, we examine the possible processes that can lead to LOB and spontaneous emission, namely, frontogenesis at the edge of the eddy and eddy instabilities. Geostrophic adjustment (Rossby 1938) is another obvious candidate for IW emission in initial value problems. However, because our solutions are statistically steady (Barkan et al. 2017), we do not specifically distinguish between geostrophic adjustment and frontogenesis (e.g., Blumen 2000).

a. Frontogenesis

To investigate the potential role of frontogenesis in the generation of IWs, as detailed in Shakespeare and Taylor (2014), we compute the correlation function between the wave kinetic

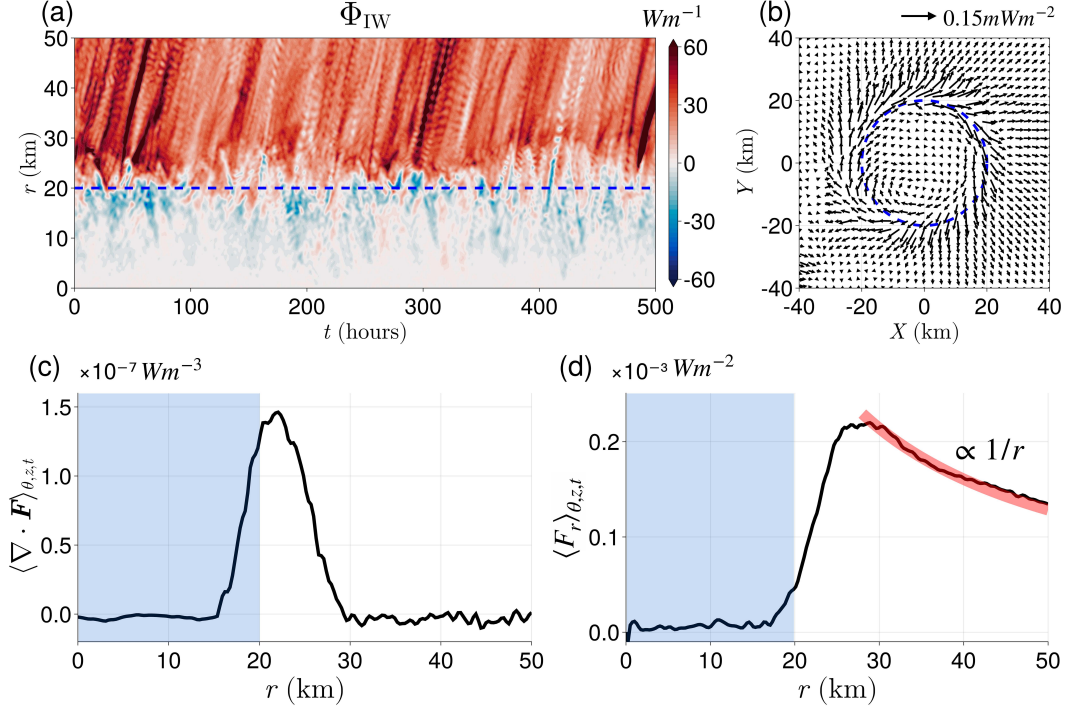


FIG. 3. (a) Radial and time-series plot of the IW energy propagation Φ_{IW} [Eq. (9)]. (b) Time and vertically averaged IW energy flux vector \mathbf{F} given by Eq. (7). The dotted blue lines in (a) and (b) indicate the edge of the anticyclonic eddy at $r = 20$ km. Azimuthal, vertical, and time average of (c) divergence of the energy flux \mathbf{F} given by Eq. (10) and (d) radial energy flux F_r . The thick red line shows the curve r^{-1} . The blue-shaded regions in (c) and (d) show the eddy region. The time average for (b)–(d) is performed over 35 inertial periods.

energy K and the frontogenetic tendency rate T_b of the mean flow buoyancy gradient:

$$\bar{C} = \frac{\langle T_b K \rangle_V}{\sqrt{\langle T_b^2 \rangle_V \langle K^2 \rangle_V}}, \quad (11)$$

where $\langle \rangle_V$ is the volume integral carried out around the edge of the eddy, i.e., $15 \leq r \leq 25$ km, and over the upper 200 m of the domain where the strain is substantial (not shown). In Eq. (11), the frontogenetic tendency rate T_b is defined (Barkan et al. 2019) as follows:

$$T_b = \frac{F_b}{|\nabla_h \bar{b}|^2}, \quad (12)$$

with F_b denoting the frontogenetic tendency for $|\nabla_h \bar{b}|$ (Hoskins 1982):

$$F_b = - \left[\frac{\partial \bar{u}}{\partial X} \left(\frac{\partial \bar{b}}{\partial X} \right)^2 + \frac{\partial \bar{v}}{\partial Y} \left(\frac{\partial \bar{b}}{\partial Y} \right)^2 + \left(\frac{\partial \bar{v}}{\partial X} + \frac{\partial \bar{u}}{\partial Y} \right) \frac{\partial \bar{b}}{\partial X} \frac{\partial \bar{b}}{\partial Y} \right], \quad (13)$$

such that positive (negative) values of T_b denote frontogenetic (frontolytic) flow regions. The wave kinetic energy is defined as

$$K = \frac{1}{2} (\bar{u}' \bar{u}' + \bar{v}' \bar{v}'). \quad (14)$$

Since K is positive definite by construction, \bar{C} is expected to be positive and close to 1 if the frontogenetic regions strongly correlate with regions of high K .

Interestingly, we find correlation \bar{C} to be slightly positive but very weak (Fig. 4c), suggesting that frontogenesis is unlikely to be the key mechanism responsible for the observed IW emission. Indeed, a representative snapshot of T_b (Fig. 4a) shows rather weak frontogenetic rates without a clear sign at the periphery of the eddy and with little spatial resemblance to the IW kinetic energy patterns (Fig. 4b).

b. Eddy instability

We examine whether the observed LOB in the numerical simulation is related to an instability of the anticyclonic eddy by examining the necessary criteria for different instabilities.

Symmetric instability (SI) can trigger LOB and, therefore, can lead to spontaneous IW emission (Chouksey et al. 2022). The necessary condition for symmetric instability requires $fQ_m < 0$ (Hoskins 1974), where f is the Coriolis frequency, and

$$Q_m = (f + \zeta_m) \partial_Z b_m - \partial_Z v_m \partial_X b_m + \partial_Z u_m \partial_Y b_m, \quad (15)$$

which is Ertel's PV of the mean flow under the hydrostatic approximation¹ and ∂_X, ∂_Y , and ∂_Z denote the derivatives in the X , Y , and Z directions, respectively. Since $Q_m > 0$ in our

¹ We solve for the nonhydrostatic equations of motion, but because of the grid spacing we use (section 2), our solutions are effectively hydrostatic.

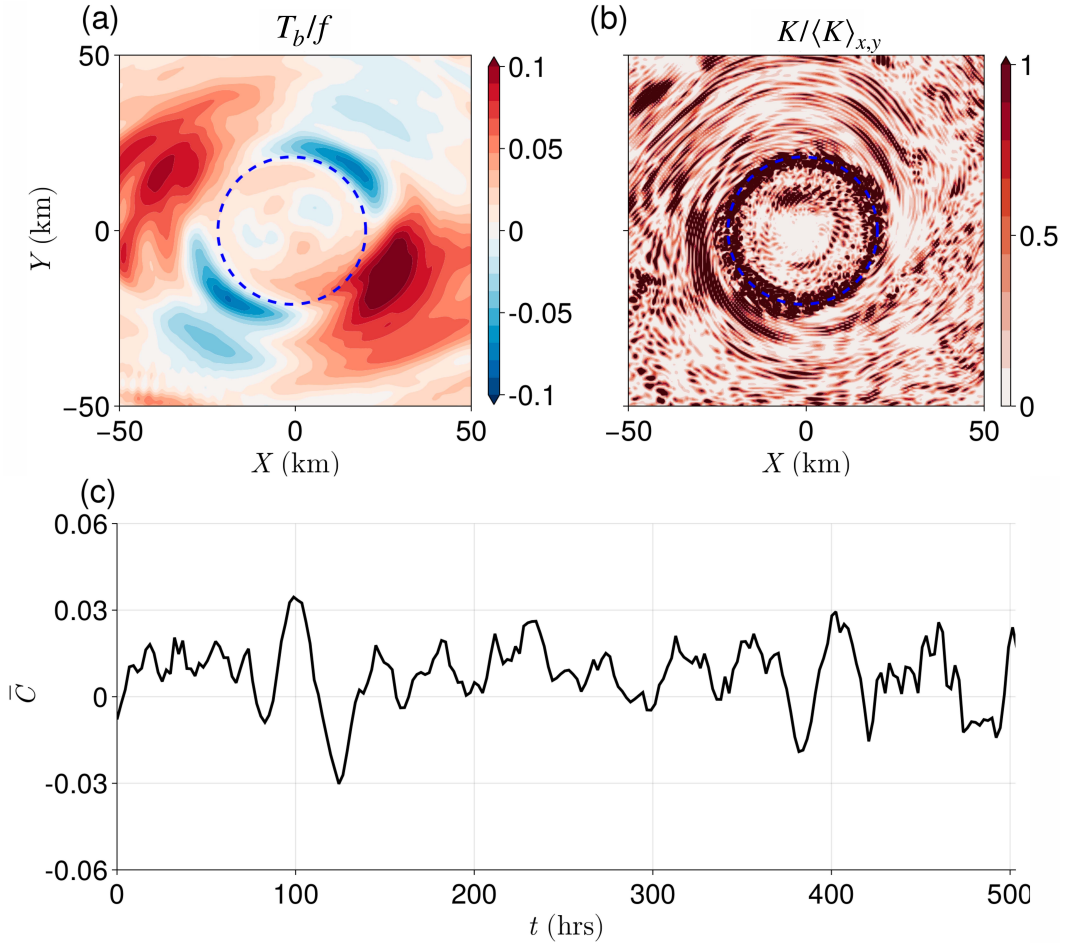


FIG. 4. A representative surface snapshot of (a) frontogenetic tendency rate T_b (normalized by f) and (b) wave KE K (normalized by the surface average $K \langle K \rangle_{x,y}$). (c) Time series of the correlation function \bar{C} [Eq. (11)] averaged over the upper 200 m of the domain. The dotted blue lines in (a) and (b) mark the edge of the eddy.

solutions ($f > 0$ in our configuration), the anticyclonic eddy is stable to SI (Fig. 5a).

McWilliams et al. (1998, 2004) derived limiting conditions for the integrability of a set of balanced equations in the isopycnal coordinates. They demonstrated that $A_m - S_m < 0$ (for $f > 0$) is a sufficient condition for LOB, where

$$A_m = f + \partial_{X_s} v_m - \partial_{Y_s} u_m, \quad (16a)$$

and

$$S_m = \sqrt{(\partial_{X_s} u_m - \partial_{Y_s} v_m)^2 + (\partial_{X_s} v_m + \partial_{Y_s} u_m)^2}, \quad (16b)$$

which denote the absolute vorticity and the magnitude of the horizontal strain rate of the balanced flow, respectively, and the spatial derivatives are computed in the isopycnal coordinate system ($X_s = X$, $Y_s = Y$, $Z_s = b_m$), namely,

$$\frac{\partial}{\partial X_s} = \frac{\partial}{\partial X} - \frac{\partial_X b_m}{\partial_Z b_m} \frac{\partial}{\partial Z}, \quad (17a)$$

$$\frac{\partial}{\partial Y_s} = \frac{\partial}{\partial Y} - \frac{\partial_Y b_m}{\partial_Z b_m} \frac{\partial}{\partial Z}. \quad (17b)$$

Ménesguen et al. (2012) and Wang et al. (2014) further showed that this LOB condition is closely related to the onset of ageostrophic anticyclonic instability (AAI), which is triggered in the neighborhood of, rather than precisely at, $A_m - S_m < 0$. The simulated anticyclonic eddy in our solutions satisfies this condition for LOB and may indeed be unstable to AAI (Fig. 5b).

The necessary condition for an inflection point instability is given by the Rayleigh–Kuo–Fjørtoft condition, which requires a sign change in the PV gradient within the domain (sometimes referred to as barotropic or lateral shear instability). In the case of a baroclinic flow (as is the case here), the necessary condition is the sign change in the along-isopycnal gradient of PV within the domain (Eliassen 1983), which is defined as

$$\partial_s \langle Q_m \rangle_\theta = \partial_r \langle Q_m \rangle_\theta - \frac{\partial_r \langle b_m \rangle_\theta}{\partial_z \langle b_m \rangle_\theta} \partial_z \langle Q_m \rangle_\theta. \quad (18)$$

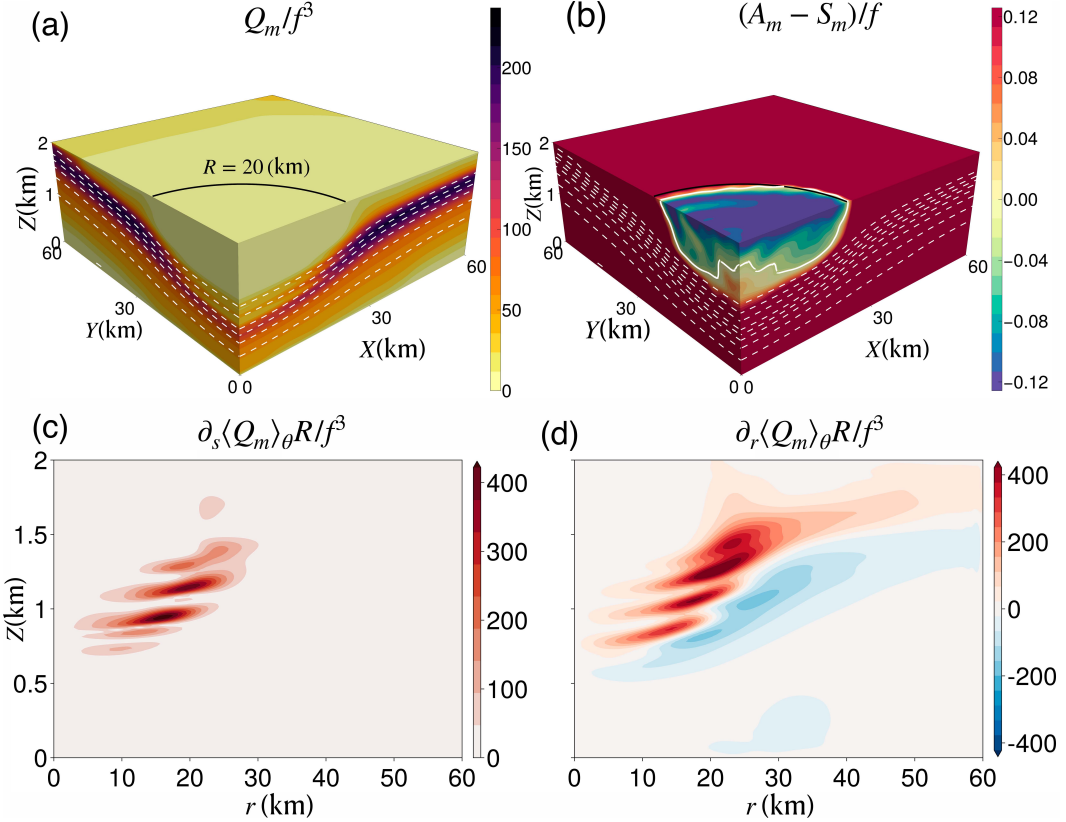


FIG. 5. Necessary criteria for instability of the basic state. (a) Mean flow PV Q_m [normalized by f^3 ; Eq. (15)]. (b) $(A_m - S_m)$ [normalized by f ; Eqs. (16a) and (16b)]. (c) Along-isopycnal PV gradient $\partial_s \langle Q_m \rangle_\theta$ [normalized by f^3/R ; Eq. (18)] and (d) radial PV gradient $\partial_r \langle Q_m \rangle_\theta$ (normalized by f^3/R). The white dotted lines in (a) and (b) show buoyancy contours with a 0.002 m s^{-2} contour interval. The solid white lines in (b) show where $\bar{A}_m - \bar{S}_m = 0$. The black line in (a) and (b) marks the edge of the anticyclonic eddy. All quantities are averaged over 24 h.

Interestingly, the azimuthal- and time-averaged $\partial_s \langle Q_m \rangle_\theta$ does not change sign within the anticyclonic eddy (Fig. 5c), whereas the azimuthal- and time-averaged $\partial_r \langle Q_m \rangle_\theta$ does (Fig. 5d). This implies that the anticyclonic eddy is stable to inflection point instability but may be unstable to barotropic (lateral shear) instability. Barotropic instability can occur within a balance model (e.g., the QG model) and, therefore, does not necessarily lead to LOB. However, if the Rossby number of the eddy is sufficiently large, the barotropic instability can become radiative. Such a radiative instability has been termed Rossby inertia buoyancy (RIB) instability (SM04; Hodyss and Nolan 2008; see section 7 for more detail).

Kelvin–Helmholtz instability (Miles 1963), which can be triggered when the Richardson number $Ri = \partial_z b_m / [(\partial_z u_m)^2 + (\partial_z v_m)^2] < 1/4$, can also lead to LOB. However, in our case, $Ri > 1/4$ is everywhere in the domain (not shown). We can further rule out centrifugal instability, which is expected to eventually lead to the breakdown of the anticyclonic eddy over rather rapid time scales (Carnevale et al. 2011). Such breakdown is not observed in the numerical simulation (see supplemental Movie 1 in the online supplemental material).

5. Linear stability analysis: Configuration and numerical methods

In the previous section, we demonstrated that the anticyclonic eddy is susceptible to AAI and barotropic shear instability. In this section, we conduct a linear stability analysis of the anticyclonic eddy to determine whether the observed spontaneous IW emission results from an instability.

Our basic state is defined with respect to the azimuthally averaged and 24-h low-pass fields (Figs. 6a,c,e), which approximately satisfy gradient wind balance (Fig. 2b). This basic state, which we refer to as case 1, satisfies the necessary condition for both AAI and lateral shear instability. In what follows, we contrast the stability analysis of the basic state in case 1 with that of a modified basic state (case 2; Figs. 6b,d,f), where we spatially low pass the normal strain components $\partial_X u_m$ and $\partial_Y v_m$ such that $(A_m - S_m) > 0$ everywhere (Fig. 6f). The low-pass filter is a sixth-order Butterworth spatial filter with a filter width of 1.5 km. This comparison helps us identify the dominant instability mechanism responsible for the spontaneous emission of IWs.

a. Governing equations

The equations of motion for the perturbation fields u_r , u_θ , w , p , and b satisfy the linearized Navier–Stokes equations on

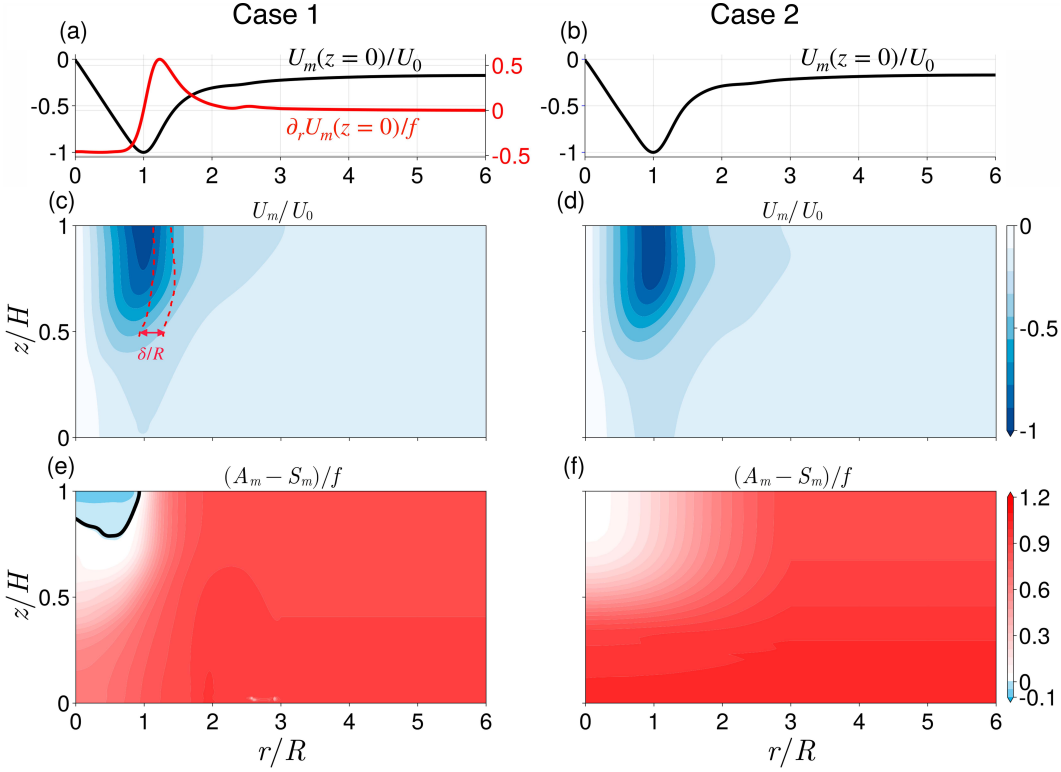


FIG. 6. The basic states used for the linear stability analysis. (a),(b) Azimuthally averaged surface azimuthal mean velocity U_m (normalized by the maximal magnitude of the eddy azimuthal velocity U_0) and (c),(d) contour plots of U_m (normalized by U_0). (e),(f) The necessary condition for AAI, where the solid black line in (e) denotes the $(A_s - S_m) = 0$ contour. (e) Case 1 corresponds to a basic state where the necessary condition for AAI is satisfied, whereas (f) case 2 corresponds to a basic state where the necessary condition for AAI is not satisfied. The red line in (a) shows the surface horizontal shear $\partial_r U_m$ (normalized by f). The red dotted lines in (c) show the shear layer thickness δ (normalized by the radius of the eddy R) computed based on radial distance corresponding to 80% of the maximum magnitude of $\partial_r U_m$.

an f plane, under the Boussinesq approximation. We use a cylindrical coordinate system centered around the anticyclonic eddy [Eq. (8)] and define the following length and time scales:

$$r = R\tilde{r}, \quad (19a)$$

$$z = H\tilde{z}, \quad (19b)$$

$$t = \frac{1}{f}\tilde{t}, \quad (19c)$$

where $R = 20$ km is the eddy radius, $H = 2$ km is the domain depth, and $f = 1.2 \times 10^{-4} \text{ s}^{-1}$ is the Coriolis frequency used in our simulations.

The velocity, pressure, and buoyancy are scaled with

$$(u_r, u_\theta) = U_0(\tilde{u}_r, \tilde{u}_\theta), \quad (20a)$$

$$w = U_0 H / R \tilde{w}, \quad (20b)$$

$$p = f U_0 R \tilde{p}, \quad (20c)$$

$$b = f U_0 R / H \tilde{b}, \quad (20d)$$

where U_0 is a characteristic velocity scale, taken to be 1.05 m s^{-1} —the maximal magnitude of the eddy azimuthal velocity. Using Eqs. (19a)–(19c) and (20a)–(20d), the equations of motion are

$$\frac{D\tilde{u}_r}{Dt} - (1 + 2\text{Ro}\tilde{\Omega})\tilde{u}_\theta = -\frac{\partial \tilde{p}}{\partial \tilde{r}} + \text{Ek} \left(\tilde{\nabla}^2 \tilde{u}_r - \frac{1}{\tilde{r}^2} \tilde{u}_r - \frac{2}{\tilde{r}^2} \frac{\partial \tilde{u}_\theta}{\partial \theta} \right), \quad (21a)$$

$$\begin{aligned} \frac{D\tilde{u}_\theta}{Dt} + (1 + \text{Ro}\tilde{\xi})\tilde{u}_r + \text{Ro}\tilde{r} \frac{\partial \tilde{\Omega}}{\partial \tilde{z}} \tilde{w} &= -\frac{1}{\tilde{r}} \frac{\partial \tilde{p}}{\partial \theta} \\ &+ \text{Ek} \left(\tilde{\nabla}^2 \tilde{u}_\theta - \frac{1}{\tilde{r}^2} \tilde{u}_\theta + \frac{2}{\tilde{r}^2} \frac{\partial \tilde{u}_r}{\partial \theta} \right), \end{aligned} \quad (21b)$$

$$\frac{D\tilde{w}}{Dt} = -\frac{1}{\alpha^2} \frac{\partial \tilde{p}}{\partial \tilde{z}} + \frac{1}{\alpha^2} \tilde{b} + \text{Ek} \tilde{\nabla}^2 \tilde{w}, \quad (21c)$$

$$\frac{D\tilde{b}}{Dt} + \text{Ro}\tilde{u} \frac{\partial \tilde{B}}{\partial \tilde{r}} + \text{Ro}\tilde{w} \frac{\partial \tilde{B}}{\partial \tilde{z}} = \frac{\text{Ek}}{\text{Pr}} \tilde{\nabla}^2 \tilde{b}, \quad (21d)$$

$$\frac{1}{\tilde{r}} \frac{\partial}{\partial \tilde{r}} (\tilde{r} \tilde{u}_r) + \frac{1}{\tilde{r}} \frac{\partial \tilde{u}_\theta}{\partial \theta} + \frac{\partial \tilde{w}}{\partial \tilde{z}} = 0, \quad (21e)$$

where $\tilde{U}_\theta = \tilde{U}_\theta/\tilde{r}$, and $\tilde{\zeta} = 1/\tilde{r}\partial/\partial\tilde{r}(\tilde{r}^2\tilde{\Omega})$ are the nondimensional azimuthal velocity, angular velocity, and vertical component of vorticity of the basic state, respectively. The Rossby number $\text{Ro} = U_0/(fR)$, and $\alpha = H/R$ is the aspect ratio of the eddy. The Ekman number $\text{Ek} = \nu/(fR^2)$ is set to be 10^{-8} (corresponding to a viscosity $\nu = 5 \times 10^{-4} \text{ m}^2 \text{ s}^{-1}$, as is used in the numerical simulation), and the Prandtl number $\text{Pr} = \nu/\kappa$ is taken to be 1, where κ is the diffusivity. The nondimensional material derivative is

$$\frac{D}{Dt} = \frac{\partial}{\partial\tilde{t}} + \text{Ro}\tilde{\Omega}\frac{\partial}{\partial\theta}, \quad (22)$$

and the Laplacian operator is

$$\tilde{\nabla}^2 = \frac{\partial^2}{\partial\tilde{r}^2} + \frac{1}{\tilde{r}}\frac{\partial}{\partial\tilde{r}} + \frac{1}{\tilde{r}^2}\frac{\partial^2}{\partial\theta^2} + \frac{1}{\alpha^2}\frac{\partial^2}{\partial\tilde{z}^2}. \quad (23)$$

We consider a normal-mode form of the perturbations:

$$[\tilde{u}_r, \tilde{u}_\theta, \tilde{w}, \tilde{p}, \tilde{b}](\tilde{r}, \theta, \tilde{z}, \tilde{t}) = \Re([\hat{u}_r, \hat{u}_\theta, \hat{w}, \hat{p}, \hat{b}](\tilde{r}, \tilde{z})e^{\tilde{\omega}\tilde{t}+im\theta}], \quad (24)$$

where \Re denotes the real part and the hat quantities denote the complex eigenfunctions, which depend on \tilde{r} and \tilde{z} . The variable m is the azimuthal wavenumber and $\tilde{\omega} = \tilde{\omega}_r + i\tilde{\omega}_i$, with $\tilde{\omega}_r$ denoting the growth rate and $\tilde{\omega}_i$ denoting the frequency of the perturbation. In what follows, we consider only the positive m values since $\tilde{\omega}(m) = \tilde{\omega}^*(-m)$, where the superscript “star” denotes the complex conjugate. The domain is $\tilde{r} \in [0, \tilde{R}_{\max}]$ and $\tilde{z} \in [0, 1]$, where $\tilde{R}_{\max} = 9$ is the maximum radial domain size (see section 5b and appendix B for more details).

The boundary conditions for the velocity and pressure at $\tilde{r} = 0$ depend on the azimuthal wavenumber m (Batchelor and Gill 1962; Khorrami et al. 1989):

$$\frac{\partial\tilde{u}_r}{\partial\tilde{r}} = \tilde{u}_r + \frac{\partial\tilde{u}_\theta}{\partial\theta} = \tilde{w} = \tilde{p} = \tilde{b} = 0, \text{ for } m = 1, \quad (25a)$$

$$\tilde{u}_r = \tilde{u}_\theta = \tilde{w} = \tilde{p} = \tilde{b} = 0, \text{ for } m \geq 2. \quad (25b)$$

The boundary conditions at $\tilde{r} = \tilde{R}_{\max}$ are given by

$$\tilde{u}_r = \tilde{u}_\theta = \tilde{w} = \tilde{p} = \tilde{b} = 0. \quad (26)$$

In accordance with the numerical solutions (i.e., Barkan et al. 2017), we choose free-slip, rigid wall, and no-flux boundary conditions in the vertical direction, i.e.,

$$\frac{\partial\tilde{u}_r}{\partial\tilde{z}} = \frac{\partial\tilde{u}_\theta}{\partial\tilde{z}} = \tilde{w} = \frac{\partial\tilde{p}}{\partial\tilde{z}} = \frac{\partial\tilde{b}}{\partial\tilde{z}} = 0, \text{ at } \tilde{z} = 0, 1. \quad (27)$$

b. Numerical methodology

Equations (21a)–(21e) are discretized using the second-order finite-difference method. The resulting discretized Eqs. (21a)–(21e), using Eq. (24), and with boundary conditions

[Eqs. (25a)–(25b), (26), and (27)] can be expressed as a standard generalized eigenvalue problem:

$$\mathbf{AX} = \tilde{\omega}\mathbf{BX}, \quad (28)$$

where $\tilde{\omega}$ is the eigenvalue and $\mathbf{X} = [\hat{u}_r, \hat{u}_\theta, \hat{w}, \hat{p}, \hat{b}]^T$ is the eigenvector. The sparse matrices \mathbf{A} and \mathbf{B} are of size $(5N_r N_z)^2$, with N_r and N_z denoting the number of grid points in the r and z directions, respectively. The eigenvalue problem in Eq. (28) is solved using the FEAST algorithm, which is based on the complex contour integration method (Polizzi 2009). In what follows, we only consider the perturbation mode with the largest growth rate for a given value of m . The benchmark of the eigensolver is discussed in appendix A.

The grid convergence results (appendix B) are obtained for the most unstable mode (i.e., $m = 7$) by varying the number of grid points from $N_z = 50$ to $N_z = 100$ while keeping the ratio $N_r/N_z = \tilde{R}_{\max}$. Convergence is obtained for $N_z = 80$ and $N_r = 720$ (Fig. B2). Furthermore, we check the sensitivity of the results to the domain size in the radial direction by comparing between $\tilde{R}_{\max} = 6$ and $\tilde{R}_{\max} = 9$ and find little difference (Fig. B1). This indicates that our results are not influenced by our choice of boundary conditions. In what follows, we present the linear stability results using $N_z = 80$, $N_r = 720$, and $\tilde{R}_{\max} = 9$.

6. Results of the stability analysis and comparison with the numerical solution

The linear stability analysis described in the previous section is carried out for the two basic states (Fig. 6) corresponding to the simulated anticyclonic eddy (case 1) and the smoothed-strain version (case 2; AAI stable). The growth rates and frequencies for different azimuthal wavenumbers are nearly identical for the two cases (Figs. 7a,b), with the most unstable modes corresponding to $m = 7$ –9 (the most unstable mode is $m = 7$ and $m = 8$ for case 1 and case 2, respectively). Furthermore, the eigenfunctions also share similar spatial structures (Figs. 7c,d), with a clear signature of a radiating IW that closely resembles the spiral-shaped IWs emanating from the edge of the eddy in the numerical solution (Figs. 1c,d). Although it is possible that some weakly unstable AAI modes are also excited in case 1 (we only look for the most unstable modes in our analysis), these findings suggest that the spontaneous IW emission in the numerical solution is likely the result of radiative instability.

a. Kinetic energy exchanges

To further establish the connection between the linear stability analysis and the numerical solution, we compare the exchange terms in the evolution equation of the perturbation KE. Due to a near-axisymmetric structure of the eddy (e.g., Fig. 1a), it is reasonable to define the perturbation quantities in the numerical simulation as the deviation from the azimuthal average. With this definition, the dominant energy exchange terms can be expressed as²

² The radial and vertical components of the mean flow are negligible compared with the azimuthal component.

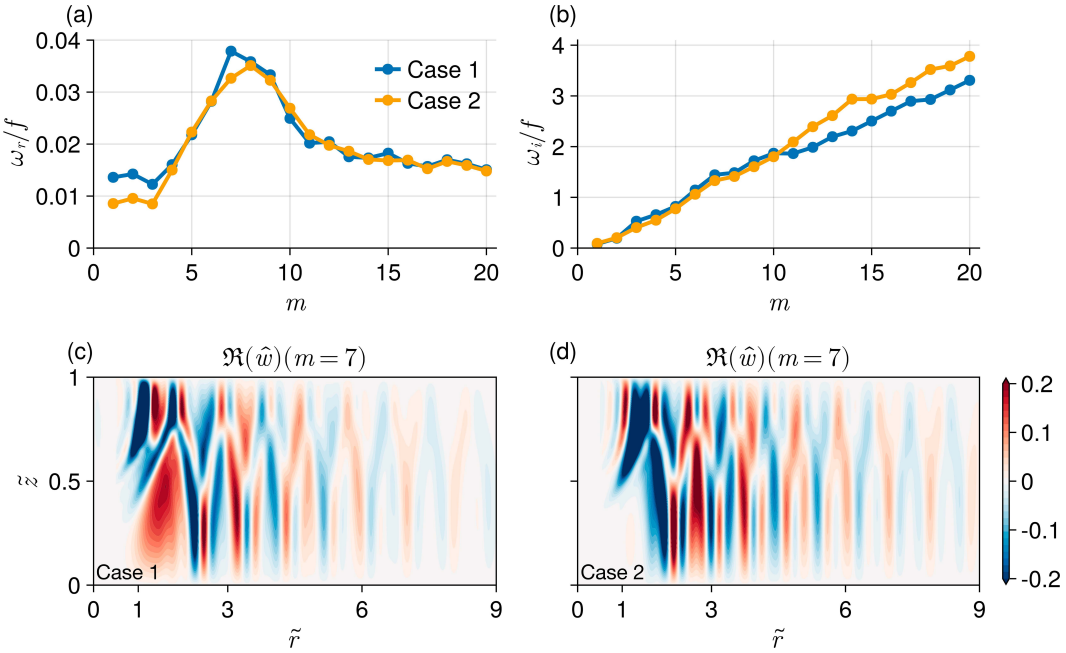


FIG. 7. (a) Nondimensional growth rate $\tilde{\omega}_r = \omega_r/f$ and (b) nondimensional frequency $\tilde{\omega}_i = \omega_i/f$ for different values of azimuthal wavenumber m , computed for the two basic states (Fig. 6). The perturbation frequency ω_i increases almost linearly with the azimuthal wavenumber m . A linear fit of the (b) data shows that the slopes of the curves (i.e., $\tilde{\omega}_i/m$) are 0.17 and 0.19 for case 1 and case 2, respectively. (c),(d) The real part of the vertical velocity eigenfunction $\Re(\hat{w})$ for the two basic states, for $m = 7$.

$$\text{HSP} = -u'_r u'_\theta \frac{\partial \langle U_\theta \rangle_\theta}{\partial r}, \quad (29a)$$

$$\text{VSP} = -w' u'_\theta \frac{\partial \langle U_\theta \rangle_\theta}{\partial z}, \quad (29b)$$

$$\text{BFLUX} = w' b', \quad (29c)$$

where $\langle U_\theta \rangle_\theta$ is the azimuthally averaged azimuthal velocity of the eddy and the primes denote perturbations from the azimuthal mean. We verified that the perturbation quantities are an order of magnitude smaller than the maximal magnitude of the azimuthal velocity, consistent with linear stability theory. The first two terms in Eqs. (29a)–(29c), horizontal shear production (HSP) and vertical shear production (VSP), are associated with the horizontal (radial) and vertical shear of the mean flow, respectively. A positive value of HSP (or VSP) describes the growth of the perturbation KE at the expense of the mean flow KE. The third term in Eqs. (29a)–(29c), the buoyancy flux (BFLUX), quantifies energy exchanges between the perturbation kinetic and potential energies.

The following perturbation KE equation—corresponding to the linear stability analysis—is obtained by substituting Eq. (24) into Eq. (21) and multiplying Eqs. (21a)–(21c), with \hat{u}^* , \hat{v}^* , and \hat{w}^* , respectively,

$$\begin{aligned} & 2\tilde{\omega}\langle K_p \rangle_\theta + \underbrace{\frac{\tilde{U}}{\tilde{r}} \langle \hat{u}_r \hat{u}_\theta^* - 2\hat{u}_r^* \hat{u}_\theta \rangle_\theta}_{\text{Curvature}} + \underbrace{\langle \hat{u}_r \hat{u}_\theta^* - \hat{u}_\theta^* \hat{u}_r \rangle_\theta}_{\text{Coriolis}} \\ & = \underbrace{-\text{Ro} \frac{\partial \tilde{U}}{\partial \tilde{r}} \langle \hat{u}_r \hat{u}_\theta^* \rangle_\theta}_{\text{HSP}^\text{stab}} - \underbrace{\text{Ro} \frac{\partial \tilde{U}}{\partial \tilde{z}} \langle \hat{w} \hat{u}_\theta^* \rangle_\theta}_{\text{VSP}^\text{stab}} + \underbrace{\langle \hat{w}^* \hat{b} \rangle_\theta}_{\text{BFLUX}^\text{stab}} + \underbrace{\tilde{\nabla} \cdot (\hat{u}^* \hat{p})_\theta}_{\text{PWORK}} \\ & + \underbrace{\text{Ek} \langle \hat{u}_r^* \tilde{\nabla}^2 \hat{u}_r - \frac{1}{\tilde{r}^2} \hat{u}_r \hat{u}_r^* + \hat{u}_\theta^* \tilde{\nabla}^2 \hat{u}_\theta - \frac{1}{\tilde{r}^2} \hat{u}_\theta \hat{u}_\theta^* + \alpha^2 \hat{w}^* \tilde{\nabla}^2 \hat{w} \rangle_\theta}_{\text{DISP}} \end{aligned} \quad (30)$$

where $K_p = 1/2(\hat{u}_r \hat{u}_r^* + \hat{u}_\theta \hat{u}_\theta^* + \alpha^2 \hat{w} \hat{w}^*)$ is the perturbation KE. The superscript “stab” is added to the HSP, VSP, and BFLUX to distinguish them from the exchange terms defined in the numerical solution [Eqs. (29a)–(29c)], but their physical interpretation remains the same. The curvature term appears due to the circular structure of the mean flow. It is purely imaginary and thus does not contribute to the growth of the perturbation KE. Similarly, the Coriolis term does not participate in the growth of the perturbation KE either. The PWORK term denotes the propagation of KE due to pressure perturbations. It has a zero domain average because there is no propagation of KE through the boundaries. The dissipation term (DISP) for the unstable perturbation is negligible (not shown).

The comparison between the energy exchange terms in the numerical solution and the linear stability analysis for case 1

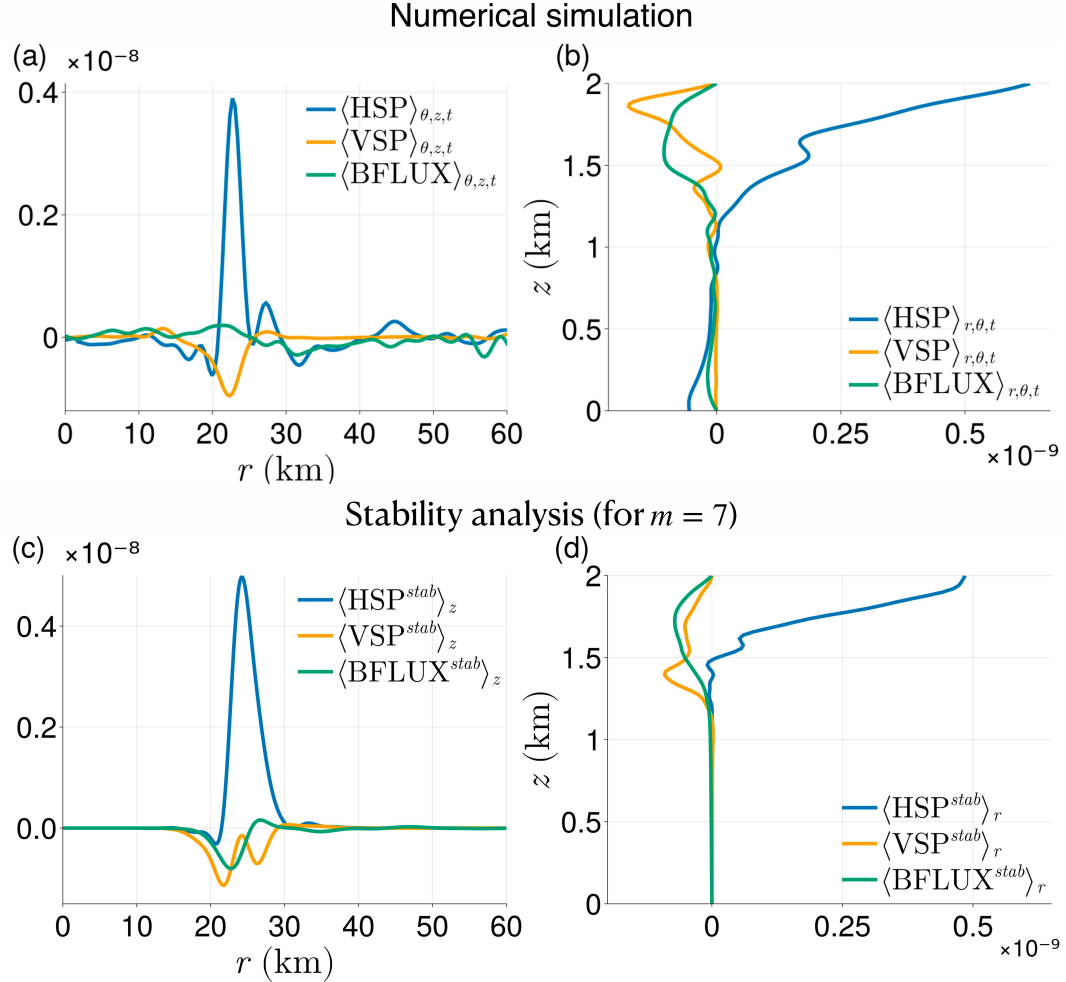


FIG. 8. A comparison of the energy exchange terms between the mean flow and the perturbation, computed (a),(b) in the numerical simulations [Eqs. (29a)–(29c)] and (c),(d) in the stability analysis of the case 1 with $m = 7$ [Eq. (30); superscript $stab$]. The HSP, VSP, and BFLUX are averaged over depth, azimuth, and time in (a) and over radius, azimuth, and time in (b). The time average in (a) and (b) is over 24 h. Similarly, HSP^{stab} , VSP^{stab} , and $BFLUX^{stab}$ are depth averaged and radially averaged in (c) and (d), respectively. The terms HSP^{stab} , VSP^{stab} , and $BFLUX^{stab}$ are dimensionalized using Eqs. (20a)–(20d). (a) The perturbation quantities in the stability analysis are multiplied with a constant, which is obtained by matching the maximal magnitude of w from the stability analysis with the maximal magnitude of w' at the radial location where HSP peaks. All quantities are expressed in units of watts per kilogram.

shows a reasonable agreement (Fig. 8). To obtain the magnitude of the energy exchange term in the stability analysis, we multiply the perturbation fields \hat{u}_r , \hat{u}_θ , \hat{w} , and \hat{b} by a constant defined such that $|\hat{w}| = |w'|$ at the radial location where the HSP peaks. The dominant KE exchange term is the HSP [Eqs. (29a)–(29c) and (30)], which is characteristic of the lateral shear instability. The radial distributions of $\langle HSP \rangle_{\theta,z,t}$ and $\langle HSP^{stab} \rangle_z$ show that the energy exchange occurs just outside of the anticyclonic eddy (Figs. 8a,c), where the horizontal shear of the mean flow is positive (e.g., red line in Fig. 6a). This is because the perturbation phase lines are tilted against the horizontal shear of the mean flow. The vertical distributions of $\langle HSP \rangle_{\theta,z,t}$ and $\langle HSP^{stab} \rangle_z$ suggest that energy exchange occurs in the upper half of the domain (Figs. 8b,d).

Méneguen et al. (2012) performed a linear stability analysis of an idealized AAI unstable basic state and showed that the AAI growing modes had equal contributions from both HSP and VSP. Since VSP is negligible in our solution (orange lines in Fig. 8) and because similar dominant energy exchange terms are found for case 2 (not shown), it is unlikely that the most unstable modes in our solution are associated with AAI.

b. Phase speed

Next, we evaluate whether the radial phase speed c_p predicted by the linear stability analysis agrees with the computed phase speed of the spontaneously emitted IWs in the numerical solution. By definition,

$$c_p = \omega_i/k_h, \quad (31)$$

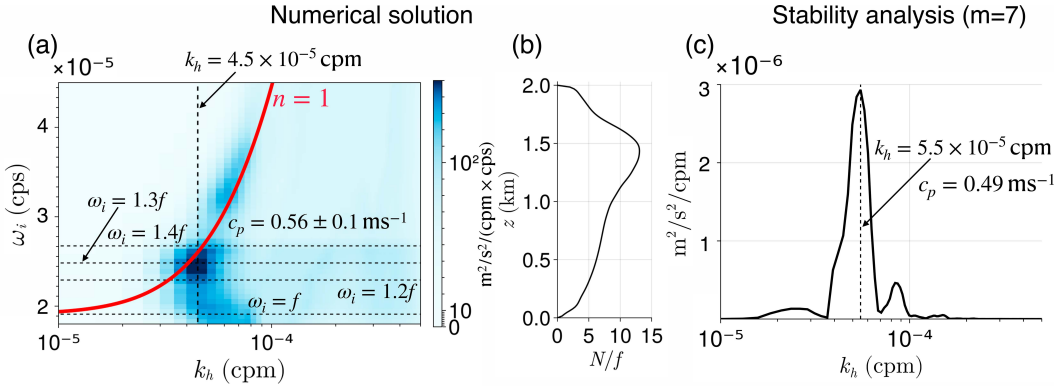


FIG. 9. (a) Frequency–horizontal wavenumber power spectral density for the modeled vertical velocity w , at $z = 1.5$ km. The solid red line represents the theoretical estimate of the dispersion relation using Eq. (33) for vertical mode $n = 1$. The horizontal dashed black lines mark the frequencies $\omega = f, 1.2f, 1.3f$, and $1.4f$. (b) The time- and horizontally averaged normalized stratification profile N/f , computed in the red box displayed in Fig. 1c, excluding the anticyclonic eddy region (time average is carried out over 35 inertial periods). (c) The horizontal wavenumber power spectral density of the vertical velocity w [using Eq. (24) at $t = 0$ after dimensionalization] at $z = 1.5$ km, based on the linear stability analysis of case 1, with $m = 7$. The power spectra density in (a) peaks in the range $1.2f < \omega_i(\text{cps}) < 1.3f$ and $4 \times 10^{-5} < k_h(\text{cpm}) < 5 \times 10^{-5}$, yielding a phase speed estimate of $c_p = 0.56 \pm 0.1 \text{ m s}^{-1}$ [Eq. (31)]. (c) The horizontal wavenumber and radial phase speed predicted by the stability analysis are $k_h = 0.49$ (cpm) and $c_p = 0.49 \text{ m s}^{-1}$, using $\omega_i = 1.42f$ ($m = 7$ in Fig. 7b).

where ω_i is the frequency and $k_h = \sqrt{k^2 + l^2}$ is the horizontal (radial) wavenumber, with k and l denoting the x and y wavenumber components, respectively.

In the numerical solution, c_p is computed by fitting the dispersion curves to the frequency–horizontal wavenumber power spectral density of the modeled vertical velocity (Fig. 9a). This is done by solving a Sturm–Liouville boundary value problem for the IW vertical modes (Gill 1982):

$$\frac{\partial}{\partial z} \left(\frac{f^2}{N^2} \frac{\partial F_n}{\partial z} \right) = -\frac{1}{R_n^2} F_n, \quad (32)$$

where F_n denotes the eigenfunction and R_n denotes the deformation radius for the n th vertical mode and subject to the boundary conditions $\partial_z F_n = 0$ at $z = 0, H$. The resulting IW dispersion relation (red line in Fig. 9a), computed from

$$\omega_i = f \sqrt{1 + R_n^2 k_h^2}, \quad (33)$$

using the time- and horizontally averaged (excluding the eddy region) buoyancy frequency N (Fig. 9b), shows a good agreement with the modeled power spectral density.

In the linear stability analysis, the frequency ω_i is calculated directly for the various unstable modes (Fig. 7b). The corresponding horizontal wavenumbers are estimated by computing the horizontal wavenumber power spectral density of the vertical velocity w for a given mode m (Fig. 9c).

The resulting k_h and associated c_p [Eq. (31)] are well within the range of the numerically computed phase speed (Figs. 9a,c), supporting the premise that the spontaneously emitted IWs result from a radiative instability of the anticyclonic eddy.

7. Discussion

The spontaneous radiation of IWs from the eddy in the numerical simulation can be understood following the RIB instability mechanism discussed in SM04. In the classical barotropic instability (e.g., Hoskins et al. 1985), the mechanism leading to perturbation growth can be rationalized as the phase locking of two counterpropagating vortex Rossby waves (VRWs),³ located in regions of opposite signs of the radial (horizontal) PV gradient. In contrast, the RIB instability mechanism described by SM04 relies on an interaction between the exterior VRW and an outward-propagating IW. Using the linear perturbation theory of a cyclonic Rankine vortex, they showed that the deformation of the vortex PV surface triggers a VRW with frequency ω_i . When $|\omega_i| > f$, the VRW excites an outward-propagating IW with the same frequency. This radiative instability relies on the existence of a critical layer, where the angular VRW phase velocity ω_i/m matches the angular velocity of the eddy Ω . The location of the critical layer is then defined by the resonance condition:

$$\Omega(r_c) = -\omega_i/m, \quad (34a)$$

$$\text{Ro}_l(r_c) = -\frac{1}{m} \frac{\omega_i}{f}, \quad (34b)$$

where $\text{Ro}_l = \Omega/f$ is the local Rossby number of the eddy. Hodyss and Nolan (2008) and Park and Billant (2012) later extended the work of SM04 and showed the prevalence of

³ VRWs are analogous to planetary Rossby waves that propagate on meridional PV gradients (Montgomery and Kallenbach 1997). The term first appeared in the context of atmospheric hurricanes (Macdonald 1968).

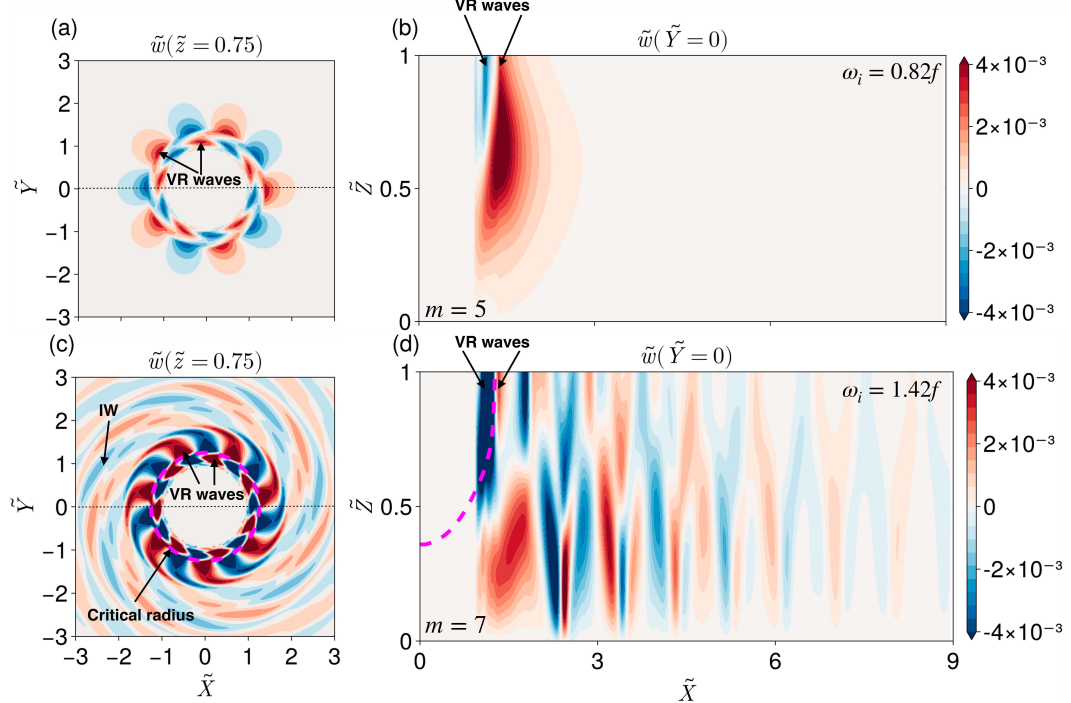


FIG. 10. Full solution of the perturbation vertical velocity \tilde{w} at $\tilde{z} = 0.75$ for case 1 from the linear stability analysis is constructed using Eq. (24) at $t = 0$ for (a),(b) $m = 5$ and (c),(d) $m = 7$. $(\tilde{X}, \tilde{Y}) = (X/R, Y/R)$. The dashed magenta lines in (c) and (d) indicate the critical radius $\tilde{r}_c(\tilde{z} = 0.75)$, where $\text{Ro}\tilde{\Omega} = -\tilde{\omega}_i/m$ [nondimensional form of Eq. (34)]. The perturbation frequency ω_i of $m = 5$ and $m = 7$ is marked at the top corner of the (b) and (d), respectively. The thin black lines in (a) and (c) show $\tilde{Y} = 0$. For $m = 5$, the perturbation frequency ω_i is a subinertial frequency; thus, there is no radiative IW. Conversely, for $m = 7$, the perturbation frequency ω_i is a superinertial frequency leading to the spiral-shaped radiative IW from the eddy.

this radiative instability in a baroclinic cyclonic eddy and a barotropic anticyclonic eddy, respectively. In the former case, the perturbation growth rate was somewhat reduced compared to the barotropic case.

In this article, we demonstrate for the first time the emergence of this radiative instability in forced-dissipative solutions of the Boussinesq equations of motion. We hypothesize that the flow field outside of the anticyclonic eddy acts to continuously perturb its PV surfaces, thereby triggering the VRWs. For illustration purposes, we contrast the eigenmode structures of two unstable modes (Fig. 10): the mode $m = 5$ —corresponding to a subinertial perturbation frequency ($\omega_i = 0.82f$; Fig. 7a), and $m = 7$ —the most unstable mode corresponding to a superinertial perturbation frequency ($\omega_i = 1.42f$; Fig. 7a).

For $m = 5$ (Figs. 10a,b), the eigenmode structure shows two radial maxima, corresponding to two counterpropagating VRWs, and no IW signature. In contrast, for $m = 7$ (Figs. 10c,d), a distinct spiral pattern of IW is visible (consistent with the numerical solution; Fig. 1c) that radiates out from the exterior VRW situated at the critical layer predicated by the SM04 mechanism [Eq. (34)]. Similarly to $m = 5$, there are still two counterpropagating VRWs that can induce mutual amplification through phase locking. However, now, the amplification of the exterior VRW can further enhance the interaction with the outward-propagating IW, thereby making

the spontaneous IW emission a self-sustained process. In contrast with SM04, we do not find clear evidence of azimuthal symmetrization of the eddy. This is potentially because SM04 is considered a Rankine vortex where the radial gradient of PV does not change sign and only a single VRW is excited. In contrast, in our solution, the PV gradient changes sign and therefore supports the mutual amplification of two counterpropagating VRWs (Fig. 10).

To estimate the magnitude of Ro_l in the vicinity of the critical layer in our solution, we consider a shear layer of thickness δ , defined based on the radial distance corresponding to 80% of the maximal radial shear magnitude at every depth (only the upper half of the domain is considered; red dotted line in Fig. 6c). The associated depth-averaged azimuthal velocity gives $|\text{Ro}_l| \approx 0.19$. This value is consistent with the observed transition from nonradiating to radiating instability occurring around $m = 5$ – 6 (Fig. 7b). Moreover, the structure of the eigenfunctions and the estimated $|\text{Ro}_l|$ are very similar for case 2 (not shown), lending further support to the interpretation of the observed insatiability as a radiative instability, following the mechanism proposed by SM04.

Finally, we emphasize that there are some discrepancies between the predictions of the linear stability analysis and the numerical simulation. In particular, the azimuthal wavenumber of the radiated IWs appears to be higher than the most

unstable mode ranges $m = 7\text{--}9$ (Figs. 1c and 7a). We do not have a clear physical explanation for this disagreement. There is undoubtedly a limit to the predictability of linear stability analysis in finite-amplitude nonlinear simulations.

8. Summary

In this study, we investigate the processes leading to spontaneous IW emission from an anticyclonic eddy in the $O(1)$ Rossby number regime. We utilize a high-resolution, forced-dissipative channel solution of the Boussinesq equations of motion and show that spontaneous LOB around the edge of the eddy closely coincides with the location of IW emission. Furthermore, we carry out perturbation KE analysis and 2D linear stability analysis of the eddy and demonstrate that the LOB and subsequent spontaneous emission occur due to radiative instability, following the mechanism proposed by SM04. To our knowledge, this is the first demonstration of this radiative instability mechanism in a forced-dissipative Boussinesq solution. In contrast with centrifugal instability (Carnevale et al. 2011) and ageostrophic anticyclonic instability (McWilliams et al. 1998; Méneguen et al. 2012), this radiative instability is not specific to anticyclonic eddies and can occur in cyclonic eddies as well, provided they are in the $O(1)$ Rossby number regime.

In our idealized, high-latitude channel solution, the spontaneous emission results in a time-averaged IW energy flux of 0.2 mW m^{-2} , which is somewhat weaker than the values reported by Alford et al. (2013), for a subtropical frontal jet. Nevertheless, if ubiquitous, this radiative instability mechanism can still provide a nonnegligible source of IW energy. To evaluate whether this mechanism can significantly reduce the eddy KE, we compute the spindown time scale:

$$t_{\text{sd}} = \frac{K_{\text{eddy}}}{H\langle\Phi_{\text{IW}}\rangle_t}, \quad (35)$$

where K_{eddy} is the eddy KE and $\langle\Phi_{\text{IW}}\rangle_t$ is the time, azimuthal, and vertical average of the radial IW energy flux (Fig. 3a). We find that $t_{\text{sd}} \approx 320$ days, suggesting that spontaneous IW emission is not an efficient mechanism for depleting eddy KE in our solutions.

To identify this mechanism in oceanic observations, it is necessary to collect measurements of the velocity field along an eddy cross section (e.g., L'Hégaret et al. 2023). This will allow us to estimate the radial shear of the azimuthal velocity $\partial\Omega/\partial r$, from which the shear layer thickness δ and the local Rossby number Ω/f can be estimated (e.g., Fig. 6c). According to our stability analysis, the azimuthal wavelength of the most unstable mode is approximately 2δ , which gives an azimuthal wavenumber $m \approx \pi R/\delta$. Thus, the instability can be of radiative type if $(\pi R/\delta)|\Omega|/f > 1$.

In our analysis, we ignored the eddy ellipticity, which has previously been shown to affect the stability characteristics under some circumstances (Ford 1994b; Plougonven and Zeitlin 2002). In addition, we have not examined the pathways of the spontaneously emitted IWs toward dissipation and mixing, through either nonlinear wave–wave interactions (e.g., McComas and Bretherton 1977) or wave–mean flow

interactions (e.g., Shakespeare and Taylor 2015; Nagai et al. 2015). Such endeavors are left for future work.

Acknowledgments. S. K. and R. B. were supported by ISF Grants 1736/18 and 2054/23. The authors report no conflicts of interest.

Data availability statement. The linear stability code used in this study is available at https://github.com/subhk/Radiative_Shear_Instability.

APPENDIX A

Benchmark of the Linear Stability Code

The stability code used in this study is benchmarked using the results of Yim et al. (2016). Yim et al. (2016) carried out a linear stability analysis of an axisymmetric eddy with azimuthal velocity U of the form:

$$U(r, z) \equiv r\Omega(r, z) = r\Omega_0 e^{-r^2/R^2 - z^2/H^2}, \quad (A1)$$

where R is the radius of the eddy, H is its half-thickness, and Ω_0 is the maximum value of its angular velocity Ω . The basic state is in gradient wind balance (Holton and Staley 1973), i.e.,

$$\left(\frac{2U}{r} + f\right)\frac{\partial U}{\partial z} = \frac{\partial B}{\partial r}, \quad (A2)$$

with

$$B(r, z) = \bar{B}(z) + \alpha^2(\Omega + f)\Omega, \quad (A3)$$

where $\bar{B}(z) = N^2 z$, the buoyancy frequency N is a positive constant, and $\alpha = H/R$. The characteristic velocity scale is $U_0 = |\Omega_0|R$ and the Rossby number $\text{Ro} = \Omega_0/f$.⁴ The Reynolds number Re is defined as $\text{Re} = (\Omega_0 R^2)/\nu = \text{Ro}/\text{Ek}$, where the Ekman number $\text{Ek} = \nu/(fR^2)$, and the Froude number is defined as $\text{Fr} = |\Omega_0|/N$. The domain size is taken to be $[0, 10R]$ and $[-5H, 5H]$. The perturbation boundary conditions at $r = 0$ and $r = R$ are similar to Eqs. (25a), (25b), and (26), respectively. The boundary condition in the vertical direction is as follows:

$$u_r = u_\theta = w = p = b = 0, \text{ at } z = -5H, 5H. \quad (A4)$$

The numbers of radial and vertical grid points are $N_r = 200$ and $N_z = 200$, respectively.

A comparison of the maximum growth rates of the perturbations for different parameters is listed in Table A1 for $m = 1$ and in Table A2 for $m = 2$. Good agreement is found with our stability code, with a maximal relative error of less than 2%. Figures A1a and A1b show the real part of the radial velocity \hat{u}_r and the azimuthal velocity \hat{u}_θ , respectively, and both velocity components compare well with Fig. 13a of Yim et al. (2016).

⁴ In Yim et al. (2016), Ro is defined as $\text{Ro} = 2\Omega_0/f$.

TABLE A1. Maximum growth rate and frequency comparisons between Yim et al. (2016) and the present stability code for $m = 1$, $\alpha = 1.2$, $Fr = 0.5$, and $Re = 10^4$ and for different values of Rossby numbers. The Yim et al. (2016) values are estimated from their Fig. 10.

Ro $\tilde{\omega}$		
Rossby No. (Ro)	Yim et al. (2016)	Present code
Ro = 5	$\approx 0.071\text{--}0.098i$	0.072–0.094i
Ro = 7.5	$\approx 0.090\text{--}0.108i$	0.091–0.101i
Ro = 10	$\approx 0.098\text{--}0.118i$	0.098–0.117i

TABLE A2. Maximum growth rate and frequency comparisons between Yim et al. (2016) and the present stability code for $m = 2$, $\alpha = 1.2$, $Fr = 0.5$, and $Re = 10^4$ and for different values of Rossby numbers. The Yim et al. (2016) values are estimated from their Fig. 15.

Ro $\tilde{\omega}$		
Rossby No. (Ro)	Yim et al. (2016)	Present code
Ro = 5	$\approx 0.017\text{--}0.233i$	0.016–0.236i
Ro = 7.5	$\approx 0.011\text{--}0.233i$	0.012–0.235i
Ro = 10	$\approx 0.008\text{--}0.233i$	0.008–0.234i

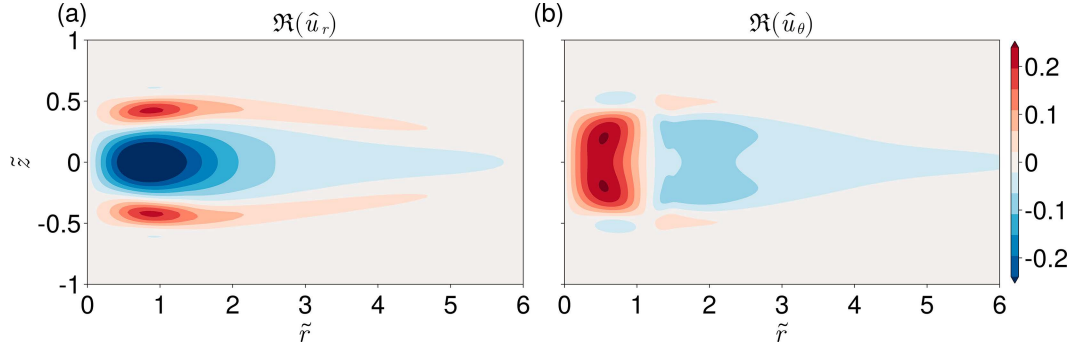


FIG. A1. The real part of (a) the radial velocity eigenfunction $\Re(\hat{u}_r)$ and (b) the azimuthal velocity eigenfunction $\Re(\hat{u}_\theta)$ for the most unstable mode ($m = 2$), with $\text{Ro} = 10$, $\alpha = 1.2$, $Fr = 0.5$, and $Re = 10^4$. These results compare well with Fig. 13a in Yim et al. (2016).

APPENDIX B

Stability Analysis Sensitivity to the Radial Domain Size and Number of Grid Points

In this section, we first test the sensitivity of the linear stability analysis to the radial domain size \tilde{R}_{\max} , by comparing two cases: $\tilde{R}_{\max} = 6$ and $\tilde{R}_{\max} = 9$. In both cases, we use $N_z = 80$ in the vertical and set $N_r/N_z = \tilde{R}_{\max}$. The eigenvalues $\tilde{\omega}$ for different values of the azimuthal wavenumber m agree well in both cases (Figs. B1a,b). Furthermore, the real part of the vertical velocity eigenfunction $\Re(\hat{w})$, based on the most unstable mode $m = 7$, exhibits a similar structure in both cases (Figs. B1c,d). This indicates that the results presented in the manuscript are converged for the maximal radial extent used ($\tilde{R}_{\max} = 9$).

Second, we determine the grid resolution convergence for the most unstable mode $m = 7$, for the AAI case (case 1 in Fig. 6). We vary the number of vertical grid points from

$N_z = 50$ to $N_z = 100$ while keeping the ratio $N_r/N_z = \tilde{R}_{\max}$, where N_r is the number of grid points in the r direction. We consider the case with $\tilde{R}_{\max} = 9$, which gives maximal matrix sizes [**A** and **B** in Eq. (28)] of 450000^2 . We take the eigenvalue $\tilde{\omega}$ corresponding to $N_z = 100$ as the ground truth and define the relative error of the growth rate $\tilde{\omega}_r$ and of the frequency $\tilde{\omega}_i$ to be

$$\delta\tilde{\omega}_r(N_z) = \frac{\tilde{\omega}_r(N_z) - \tilde{\omega}_r(N_z = 100)}{\tilde{\omega}_r(N_z = 100)}, \quad (\text{B1a})$$

$$\delta\tilde{\omega}_i(N_z) = \frac{\tilde{\omega}_i(N_z) - \tilde{\omega}_i(N_z = 100)}{\tilde{\omega}_i(N_z = 100)}. \quad (\text{B1b})$$

For $N_z \geq 70$, we obtain a relative error of $\leq 5\%$ for both $\tilde{\omega}_r$ and $\tilde{\omega}_i$ (Figs. B2a,b). The results presented in this manuscript are therefore calculated for $N_z = 80$ and $\tilde{R}_{\max} = 9$.

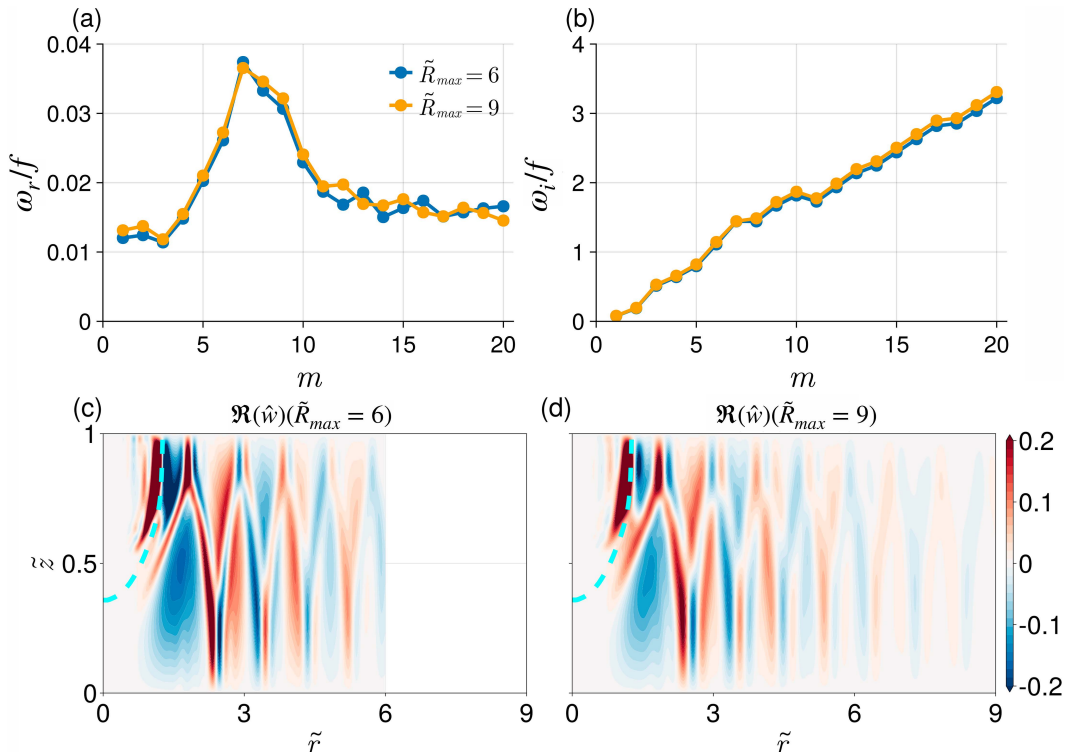


FIG. B1. A comparison of (a) the nondimensional growth rate $\tilde{\omega}_r = \omega_r/f$ and (b) the nondimensional frequency $\tilde{\omega}_i = \omega_i/f$ for the cases with $\tilde{R}_{\max} = 6, 9$ (blue and yellow lines, respectively). (c),(d) The real part of the vertical velocity eigenfunction $\Re(\hat{w})$ for the most unstable azimuthal wavenumber $m = 7$, for $\tilde{R}_{\max} = 6$ and $\tilde{R}_{\max} = 9$, respectively. The cyan line shows the critical radius $\tilde{r}_c(\tilde{z})$ given by Eq. (34). Note that the figure in (c) is plotted until $\tilde{r} = 9$ for ease of comparison.

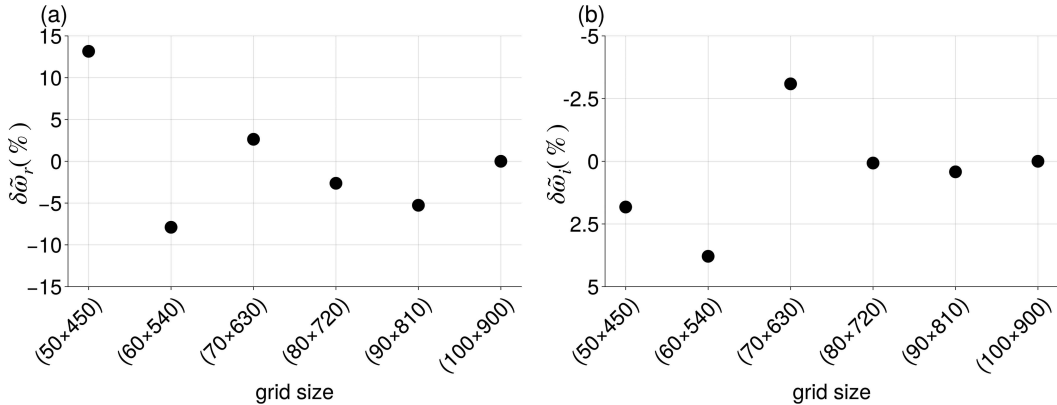


FIG. B2. Grid convergence test for the linear stability analysis of the most unstable mode ($m = 7$) and with $R_{\max} = 9$. Relative errors of (a) the growth rate $\tilde{\omega}_r$ and (b) frequency $\tilde{\omega}_i$ [Eqs. (1a) and (1b)] are presented for different grid sizes ($N_z \times N_r$).

REFERENCES

- Alford, M. H., 2003: Improved global maps and 54-year history of wind-work on ocean inertial motions. *Geophys. Res. Lett.*, **30**, 1424, <https://doi.org/10.1029/2002GL016614>.
- , A. Y. Shcherbina, and M. C. Gregg, 2013: Observations of near-inertial internal gravity waves radiating from a frontal jet. *J. Phys. Oceanogr.*, **43**, 1225–1239, <https://doi.org/10.1175/JPO-D-12-0146.1>.
- Barkan, R., K. B. Winters, and J. C. McWilliams, 2017: Stimulated imbalance and the enhancement of eddy kinetic energy dissipation by internal waves. *J. Phys. Oceanogr.*, **47**, 181–198, <https://doi.org/10.1175/JPO-D-16-0117.1>.
- , M. J. Molemaker, K. Srinivasan, J. C. McWilliams, and E. A. D’Asaro, 2019: The role of horizontal divergence in submesoscale frontogenesis. *J. Phys. Oceanogr.*, **49**, 1593–1618, <https://doi.org/10.1175/JPO-D-18-0162.1>.
- Batchelor, G. K., and A. E. Gill, 1962: Analysis of the stability of axisymmetric jets. *J. Fluid Mech.*, **14**, 529–551, <https://doi.org/10.1017/S0022112062001421>.
- Blumen, W., 2000: Inertial oscillations and frontogenesis in a zero potential vorticity model. *J. Phys. Oceanogr.*, **30**, 31–39, [https://doi.org/10.1175/1520-0485\(2000\)030<0031:IOAFIA>2.0.CO;2](https://doi.org/10.1175/1520-0485(2000)030<0031:IOAFIA>2.0.CO;2).
- Capet, X., J. C. McWilliams, M. J. Molemaker, and A. F. Shchepetkin, 2008: Mesoscale to submesoscale transition in the California Current System. Part II: Frontal processes. *J. Phys. Oceanogr.*, **38**, 44–64, <https://doi.org/10.1175/2007JPO3672.1>.
- Carnevale, G. F., R. C. Kloosterziel, P. Orlandi, and D. D. J. A. van Sommeren, 2011: Predicting the aftermath of vortex breakup in rotating flow. *J. Fluid Mech.*, **669**, 90–119, <https://doi.org/10.1017/S0022112010004945>.
- Chouksey, M., C. Eden, and D. Olbers, 2022: Gravity wave generation in balanced sheared flow revisited. *J. Phys. Oceanogr.*, **52**, 1351–1362, <https://doi.org/10.1175/JPO-D-21-0115.1>.
- Chunchuzov, I. P., O. M. Johannessen, and G. O. Marmorino, 2021: A possible generation mechanism for internal waves near the edge of a submesoscale eddy. *Tellus*, **73A**, 1947610, <https://doi.org/10.1080/16000870.2021.1947610>.
- Egbert, G. D., and R. D. Ray, 2000: Significant dissipation of tidal energy in the deep ocean inferred from satellite altimeter data. *Nature*, **405**, 775–778, <https://doi.org/10.1038/35015531>.
- Eliassen, A., 1983: The Charney-Stern theorem on barotropic-baroclinic instability. *Pure Appl. Geophys.*, **121**, 563–572, <https://doi.org/10.1007/BF02590155>.
- Ford, R., 1994a: Gravity wave radiation from vortex trains in rotating shallow water. *J. Fluid Mech.*, **281**, 81–118, <https://doi.org/10.1017/S0022112094003046>.
- , 1994b: The response of a rotating ellipse of uniform potential vorticity to gravity wave radiation. *Phys. Fluids*, **6**, 3694–3704, <https://doi.org/10.1063/1.868360>.
- , M. E. McIntyre, and W. A. Norton, 2000: Balance and the slow quasimaniifold: Some explicit results. *J. Atmos. Sci.*, **57**, 1236–1254, [https://doi.org/10.1175/1520-0469\(2000\)057<1236:BQS>2.0.CO;2](https://doi.org/10.1175/1520-0469(2000)057<1236:BQS>2.0.CO;2).
- Garabato, A. C. N., K. L. Polzin, B. A. King, K. J. Heywood, and M. Visbeck, 2004: Widespread intense turbulent mixing in the Southern Ocean. *Science*, **303**, 210–213, <https://doi.org/10.1126/science.1090929>.
- Gill, A. E., 1982: *Atmosphere–Ocean Dynamics*. Vol. 30, Academic Press, 662 pp.
- Hodyss, D., and D. S. Nolan, 2008: The Rossby-inertia-buoyancy instability in baroclinic vortices. *Phys. Fluids*, **20**, 096602, <https://doi.org/10.1063/1.2980354>.
- Holton, J. R., and D. O. Staley, 1973: An introduction to dynamic meteorology. *Amer. J. Phys.*, **41**, 752–754, <https://doi.org/10.1119/1.1987371>.
- Hoskins, B. J., 1974: The role of potential vorticity in symmetric stability and instability. *Quart. J. Roy. Meteor. Soc.*, **100**, 480–482, <https://doi.org/10.1002/qj.49710042520>.
- , 1982: The mathematical theory of frontogenesis. *Annu. Rev. Fluid Mech.*, **14**, 131–151, <https://doi.org/10.1146/annurev.fl.14.010182.001023>.
- , M. E. McIntyre, and A. W. Robertson, 1985: On the use and significance of isentropic potential vorticity maps. *Quart. J. Roy. Meteor. Soc.*, **111**, 877–946, <https://doi.org/10.1002/qj.49711147002>.
- Johannessen, O. M., S. Sandven, I. P. Chunchuzov, and R. A. Shuchman, 2019: Observations of internal waves generated by an anticyclonic eddy: A case study in the ice edge region of the Greenland Sea. *Tellus*, **71A**, 1652881, <https://doi.org/10.1080/16000870.2019.1652881>.
- Khorrami, M. R., M. R. Malik, and R. L. Ash, 1989: Application of spectral collocation techniques to the stability of swirling

- flows. *J. Comput. Phys.*, **81**, 206–229, [https://doi.org/10.1016/0021-9991\(89\)90071-5](https://doi.org/10.1016/0021-9991(89)90071-5).
- L'Hégaret, P., and Coauthors, 2023: Ocean cross-validated observations from R/Vs *L'Atalante*, *Maria S. Merian*, and *Meteor* and related platforms as part of the EUREC⁴A-OA/ATOMIC campaign. *Earth Syst. Sci. Data*, **15**, 1801–1830, <https://doi.org/10.5194/essd-15-1801-2023>.
- Lighthill, M. J., 1954: On sound generated aerodynamically II. Turbulence as a source of sound. *Proc. Roy. Soc. London, A* **222** (1148), 1–32, <https://doi.org/10.1098/rspa.1954.0049>.
- Macdonald, N. J., 1968: The evidence for the existence of Rossby-like waves in the hurricane vortex. *Tellus*, **20A**, 138–150, <https://doi.org/10.3402/tellusa.v20i1.9993>.
- McComas, C. H., and F. P. Bretherton, 1977: Resonant interaction of oceanic internal waves. *J. Geophys. Res.*, **82**, 1397–1412, <https://doi.org/10.1029/JC082i009p01397>.
- McWilliams, J. C., 1985: A uniformly valid model spanning the regimes of geostrophic and isotropic, stratified turbulence: Balanced turbulence. *J. Atmos. Sci.*, **42**, 1773–1774, [https://doi.org/10.1175/1520-0469\(1985\)042<1773:AUTVMST>2.0.CO;2](https://doi.org/10.1175/1520-0469(1985)042<1773:AUTVMST>2.0.CO;2).
- , I. Yavneh, M. J. P. Cullen, and P. R. Gent, 1998: The breakdown of large-scale flows in rotating, stratified fluids. *Phys. Fluids*, **10**, 3178–3184, <https://doi.org/10.1063/1.869844>.
- , M. J. Molemaker, and I. Yavneh, 2004: Ageostrophic, anticyclonic instability of a geostrophic, barotropic boundary current. *Phys. Fluids*, **16**, 3720–3725, <https://doi.org/10.1063/1.1785132>.
- Ménesguen, C., J. C. McWilliams, and M. J. Molemaker, 2012: Ageostrophic instability in a rotating stratified interior jet. *J. Fluid Mech.*, **711**, 599–619, <https://doi.org/10.1017/jfm.2012.412>.
- Miles, J. W., 1963: On the stability of heterogeneous shear flows. Part 2. *J. Fluid Mech.*, **16**, 209–227, <https://doi.org/10.1017/S0022112063000707>.
- Montgomery, M. T., and R. J. Kallenbach, 1997: A theory for vortex Rossby-waves and its application to spiral bands and intensity changes in hurricanes. *Quart. J. Roy. Meteor. Soc.*, **123**, 435–465, <https://doi.org/10.1002/qj.49712353810>.
- Munk, W., and C. Wunsch, 1998: Abyssal recipes II: Energetics of tidal and wind mixing. *Deep-Sea Res. I*, **45**, 1977–2010, [https://doi.org/10.1016/S0967-0637\(98\)00070-3](https://doi.org/10.1016/S0967-0637(98)00070-3).
- Nagai, T., A. Tandon, E. Kunze, and A. Mahadevan, 2015: Spontaneous generation of near-inertial waves by the Kuroshio front. *J. Phys. Oceanogr.*, **45**, 2381–2406, <https://doi.org/10.1175/JPO-D-14-0086.1>.
- Nycander, J., 2005: Generation of internal waves in the deep ocean by tides. *J. Geophys. Res.*, **110**, C10028, <https://doi.org/10.1029/2004JC002487>.
- Park, J., and P. Billant, 2012: Radiative instability of an anticyclonic vortex in a stratified rotating fluid. *J. Fluid Mech.*, **707**, 381–392, <https://doi.org/10.1017/jfm.2012.286>.
- Pedlosky, J., 2013: *Geophysical Fluid Dynamics*. Springer, 710 pp.
- Plougonven, R., and V. Zeitlin, 2002: Internal gravity wave emission from a pancake vortex: An example of wave-vortex interaction in strongly stratified flows. *Phys. Fluids*, **14**, 1259–1268, <https://doi.org/10.1063/1.1448297>.
- Polizzi, E., 2009: Density-matrix-based algorithm for solving eigenvalue problems. *Phys. Rev.*, **79**, 115112, <https://doi.org/10.1103/PhysRevB.79.115112>.
- Rama, J., C. J. Shakespeare, and A. M. Hogg, 2022: Importance of background vorticity effect and Doppler shift in defining near-inertial internal waves. *Geophys. Res. Lett.*, **49**, e2022GL099498, <https://doi.org/10.1029/2022GL099498>.
- Rimac, A., J.-S. von Storch, C. Eden, and H. Haak, 2013: The influence of high-resolution wind stress field on the power input to near-inertial motions in the ocean. *Geophys. Res. Lett.*, **40**, 4882–4886, <https://doi.org/10.1002/grl.50929>.
- Rossby, C.-G., 1938: On the mutual adjustment of pressure and velocity distributions in certain simple current systems, II. *J. Mar. Res.*, **1**, 239–267.
- Schecter, D. A., and M. T. Montgomery, 2004: Damping and pumping of a vortex Rossby wave in a monotonic cyclone: Critical layer stirring versus inertia-buoyancy wave emission. *Phys. Fluids*, **16**, 1334–1348, <https://doi.org/10.1063/1.1651485>.
- Shakespeare, C. J., and J. Taylor, 2014: The spontaneous generation of inertia-gravity waves during frontogenesis forced by large strain: Theory. *J. Fluid Mech.*, **757**, 817–853, <https://doi.org/10.1017/jfm.2014.514>.
- , and —, 2015: The spontaneous generation of inertia-gravity waves during frontogenesis forced by large strain: Numerical solutions. *J. Fluid Mech.*, **772**, 508–534, <https://doi.org/10.1017/jfm.2015.197>.
- , and A. M. Hogg, 2017: Spontaneous surface generation and interior amplification of internal waves in a regional-scale ocean model. *J. Phys. Oceanogr.*, **47**, 811–826, <https://doi.org/10.1175/JPO-D-16-0188.1>.
- Vanneste, J., 2008: Exponential smallness of inertia-gravity wave generation at small Rossby number. *J. Atmos. Sci.*, **65**, 1622–1637, <https://doi.org/10.1175/2007JAS2494.1>.
- , 2013: Balance and spontaneous wave generation in geophysical flows. *Annu. Rev. Fluid Mech.*, **45**, 147–172, <https://doi.org/10.1146/annurev-fluid-011212-140730>.
- , and I. Yavneh, 2004: Exponentially small inertia-gravity waves and the breakdown of quasigeostrophic balance. *J. Atmos. Sci.*, **61**, 211–223, [https://doi.org/10.1175/1520-0469\(2004\)061<0211:ESIWAT>2.0.CO;2](https://doi.org/10.1175/1520-0469(2004)061<0211:ESIWAT>2.0.CO;2).
- Voelker, G. S., P. G. Myers, M. Walter, and B. R. Sutherland, 2019: Generation of oceanic internal gravity waves by a cyclonic surface stress disturbance. *Dyn. Atmos. Oceans*, **86**, 116–133, <https://doi.org/10.1016/j.dynatmoce.2019.03.005>.
- Wang, P., J. C. McWilliams, and C. Ménesguen, 2014: Ageostrophic instability in rotating, stratified interior vertical shear flows. *J. Fluid Mech.*, **755**, 397–428, <https://doi.org/10.1017/jfm.2014.426>.
- Whalen, C. B., C. de Lavergne, A. C. Naveira Garabato, J. M. Klymak, J. A. MacKinnon, and K. L. Sheen, 2020: Internal wave-driven mixing: Governing processes and consequences for climate. *Nat. Rev. Earth Environ.*, **1**, 606–621, <https://doi.org/10.1038/s43017-020-0097-z>.
- Williams, P. D., T. W. N. Haine, and P. L. Read, 2008: Inertia-gravity waves emitted from balanced flow: Observations, properties, and consequences. *J. Atmos. Sci.*, **65**, 3543–3556, <https://doi.org/10.1175/2008JAS2480.1>.
- Winters, K. B., and A. de la Fuente, 2012: Modelling rotating stratified flows at laboratory-scale using spectrally-based DNS. *Ocean Modell.*, **49–50**, 47–59, <https://doi.org/10.1016/j.ocemod.2012.04.001>.
- Yim, E., P. Billant, and C. Ménesguen, 2016: Stability of an isolated pancake vortex in continuously stratified-rotating fluids. *J. Fluid Mech.*, **801**, 508–553, <https://doi.org/10.1017/jfm.2016.402>.